A time domain optical coherence tomograph for laboratory investigations on phantoms and human skin

Utveckling av en tidsupplöst optisk koherenstomograf för undersökning av fantom och hud
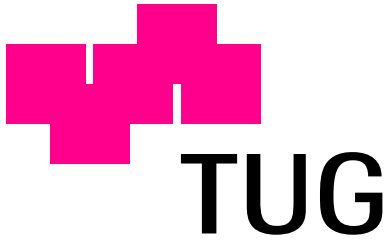
Manuel Freiberger

29 August 2005

LiTH-IMT/BIT20-EX- -05/407- -SE

Linköpings universitet
Institutionen för medicinsk teknik
Universitetssjukhuset, 581 85 Linköping, Sweden

Technische Universität Graz
Institut für Medizintechnik
Krenngasse 37 A, 8010 Graz, Austria

A time domain optical coherence tomograph for laboratory investigations on phantoms and human skin

Manuel Freiberger

Examiner at Linköping University
Prof. E. Göran Salerud

Examiner at Graz University of Technology
Prof. Hermann Scharfetter

Linköping, 29 August 2005

Linköpings tekniska högskola Institutionen för medicinsk teknik	**Rapportnr:** LiTH-IMT/BIT20-EX--05/407--SE **Datum:** 2005-08-29	

Svensk titel:
Utveckling av en tidsupplöst optisk koherenstomograf för undersökning av fantom och hud

Engelsk titel:
A time domain optical coherence tomograph for laboratory investigations on phantoms and human skin

Författare:
Manuel Freiberger

Uppdragsgivare:	**Rapporttyp:**	**Rapportspråk:**
Linköpings universitet	Examensarbete	Engelskt

Sammanfattning:
Optical coherence tomography is an imaging modality with an outstanding resolution. During the project, a time domain OCT system based on a Michelson fibre interferometer was implemented and put into operation. A super-luminescent diode with a centre wavelength of 1 295 nm and a bandwidth of 45 nm was selected as light source and a linear variable delay line as reference. Basic tests were made on phantoms constructed of filter foils and on gel-like agar slices with optical properties similar to human tissue. It was shown that the achievable resolution was at least 36 μm and can be increased. The system can easily be enhanced to create two-dimensional images.

Nyckelord:
Optical coherence tomography, low-coherence interferometry, medical imaging, imaging phantoms, Michelson interferometer

Bibliotekets anteckningar:

Abstract

Optical coherence tomography is an imaging modality with an outstanding resolution. During the project, a time domain OCT system based on a Michelson fibre interferometer was implemented and put into operation. A super-luminescent diode with a centre wavelength of 1 295 nm and a bandwidth of 45 nm was selected as light source and a linear variable delay line as reference. Basic tests were made on phantoms constructed of filter foils and on gel-like agar slices with optical properties similar to human tissue. It was shown that the achievable resolution was at least 36 µm and can be increased. The system can easily be enhanced to create two-dimensional images.

Keywords

Optical coherence tomography, low-coherence interferometry, medical imaging, imaging phantoms, Michelson interferometer

Zusammenfassung

Optische Kohärenztomographie ist ein bildgebendes Verfahren mit einer hervorragenden räumlichen Auflösung. Im Laufe des Projekts wurde ein OCT-System basierend auf einem faseroptischen Michelson-Interferometer implementiert und in Betrieb genommen. Als Lichtquelle wurde eine Superlumineszenzdiode mit einer Mittenwellenlänge von 1 295 nm und einer Bandbreite von 45 nm gewählt. Eine variable optische Verzögerungsleitung diente als Referenz. Erste Messungen an Filterfolien und gelähnlichen Agarphantomen, die die optischen Eigenschaften von menschlichem Gewebe nachbildeten, lieferten eine räumliche Auflösung von mindestens 36 µm. Durch die modulare Bauweise ist das System leicht für zweidimensionale Aufnahmen erweiterbar.

Schlüsselwörter

Optische Kohärenztomographie, Teilkohärenz-Interferometrie, medizinische Bildgebung, Gewebephantome, Michelson-Interferometer

Acknowledgements

Right at the beginning, I would like to express my sincere gratitude to my supervisor, professor E. Göran Salerud, who suggested this thesis. He would always help me along and come up with advice, but also give me the freedom to work autonomously in large part.

Michail Ilias was instrumental in realising this project. Not only had he to give up half of his room, I also bothered him with all my job-related and personal problems. Many thanks for building me up when something went wrong, and bringing me down to earth when I felt too enthusiastic.

Martin Eneling was the critical voice, the advocatus diaboli, who alluded to insufficiencies in the project, and thus lots of improvements happened on his account. Furthermore, his sunny nature brought colour into the everyday live.

The people on IMT did their best to make my stay as enjoyable as possible. To name a few representatives, there was Erik, who lent lots of great stuff to me, Daniel who threw in irrelevant German words into our discussions and Linda, Amir and Johan who built me up physically. The numerous cups of coffee together, going along with chats about all the world and his brother, not only influenced my liver but also extended the horizon.

Anja, Auntschi, Elke, Petra, Christian, Edi, Joe and Tom were the link to my home while Anna and Matilda made me experience the country and its people. My dear friends, never shall I forget the great time in Sweden I could spend with you.

Also in Austria many friends paid attention that there was more in my life than just my studies. Among others, I want to thank Boglárka, Bertl, Franz, Flo, Jakob, Ute and Wolfgang for the good time we had together.

Thousand thanks go to my parents, my sisters and my relatives for all their financial and immaterial support during my whole life and thus enabling my studies. I also appreciate the surprise visit just to see the presentation.

Last but not least, I want to thank all the people I have forgotten to mention here. It does not mean that I do not appreciate your friendship, but is evidence of my limited brain capacity.

Linköping, August 2005

Manuel Freiberger

Contents

List of Tables

List of Figures

Abbreviations and symbols

a. u.	Arbitrary units
c	Speed of light
eq.	Equation
f_0	Electrical centre frequency of the OCT signal
fig.	Figure
g	Anisotropy
i_P	Photo current
l_C	Round trip coherence length
n	Index of refraction
v_M	Motor speed
A/D	Analogue-to-digital
C_i	Concentration of the substance i
DC	Direct current
DLL	Dynamic Link Library
E_i	Electrical field of signal i
$\mathcal{F}\{\cdot\}$	Fourier transform
$\mathcal{F}^{-1}\{\cdot\}$	Inverse Fourier transform
FWHM	Full-width at half-maximum
GRIN	Gradient index
$\mathcal{H}\{\cdot\}$	Hilbert transform
I	Intensity
$\overline{I}$	Time-averaged intensity
$\hat{I}$	Envelope of the intensity
NA	Numerical aperture
OCT	Optical coherence tomography
PWM	Pulse width modulation
$\mathcal{R}\{\cdot\}$	Real part
S_{src}	Power spectrum of the light source

SMF	Single mode fibre
SNR	Signal-to-noise ratio
TEC	Thermoelectric cooler/cooling
$V(z)$	Analytic continuation of the intensity
λ_0	Centre wavelength of the light source
μ_a	Absorption coefficient
μ_s	Scattering coefficient
μ_s'	Reduced scattering coefficient
ξ	Conversion factor between intensity and electrical field
ω_0	Centre frequency of the light source
Γ_{src}	Autocorrelation function of the source
Γ_{ij}	Mutual coherence function of signals i and j
Δf	FWHM electrical bandwidth
$\Delta \lambda$	FWHM spectral bandwidth
Δt	Time delay
Δz	Difference in path lengths
$\Delta \omega$	FWHM bandwidth
$(\cdot)^*$	Complex conjugate
$\langle \cdot \rangle$	Time average

Chapter 1.

Introduction

Nowadays, several tomographic imaging techniques are established in medicine, which make use of e.g. ultrasound, X-ray and magnetic resonance. Each method measures different physical properties of tissue, has a different penetration depth and resolution in its images and is therefore suitable for special applications[1].

Computer tomography can achieve high resolutions but uses ionising radiation and bears an inherent risk. Magnetic resonance imaging does not involve such a risk, but in exchange it cannot resolve objects smaller than ca. 0.3 mm[2]. Ultrasound has a depth resolution of approximately a few wavelengths[3]. Thus even high-frequency ultrasound of 50 MHz is limited to 30 µm. Furthermore, it needs a good transport medium such as gel since sound waves are highly attenuated in air.

Optical measurement methods are an alternative to the techniques mentioned before. They are especially advantageous if high resolutions are necessary or if contact-less measurements are desired as it is the case in ophthalmology.

In histopathology, resolutions are needed which lie, according to Brezinski and Fujimoto[4], even below the detection limit of high-frequency ultrasound. If furthermore conventional biopsy is hazardous, like for example in the brain or in coronary arteries, optical coherence tomography (OCT) has good potential.

1.1. Motivation

OCT was not available at the Department of Biomedical Engineering at Linköping University. At the department, much effort is put in developing and enhancing bio-optical measurement techniques.

Optical coherence tomography can be seen as a complementary imaging modality, which yields high-resolution images of anatomical structures.

1.2. Aim of this thesis

The aim of this thesis was to implement an A-scan imaging OCT system, using a super-luminescent diode and fibre optics, for laboratory use, capable of measurement on human tissue and test phantoms.

Chapter 2.

Theoretical background

This chapter provides basic knowledge of OCT, first in an intuitive way by comparing it to ultrasound and thereafter in a more mathematical way. As the setup is designed to be used on human tissue, its optical properties are of importance and will be described, therefore.

2.1. Basic principle of OCT

As done by Fujimoto[5], optical coherence tomography is often compared to ultrasound A-mode since this is a well-known modality to gather one-dimensional information of tissue structures.

Sound waves are sent into the tissue, where they are reflected and backscattered before being detected. The depth of the reflection's origin can be calculated from the time-of-flight of the echo. Its intensity is a measure of the difference in the acoustic properties of the tissue discontinuity.

In OCT, light is used instead of sound waves. Therefore, the transport media can be omitted which is advantageous in ophthalmology. The detection limit lies in the micrometre range and is thus increased by a factor of 10 owing to the shorter wavelength[5].

However, the major problem that arises is the measurement of the time-of-flight as light waves propagate 10^5–10^6 times faster than sound waves. It is very difficult or even impossible to design electronic circuits that can reach such a speed[5].

One solution is low-coherence interferometry: one beam is split in two beams which take different paths. The beams are later recombined again. They will produce an interference signal, which is visible as fringes, for example, if, and

only if, the path difference of the two beams is smaller than the coherence length of the light source[6] (see figure 2.1).
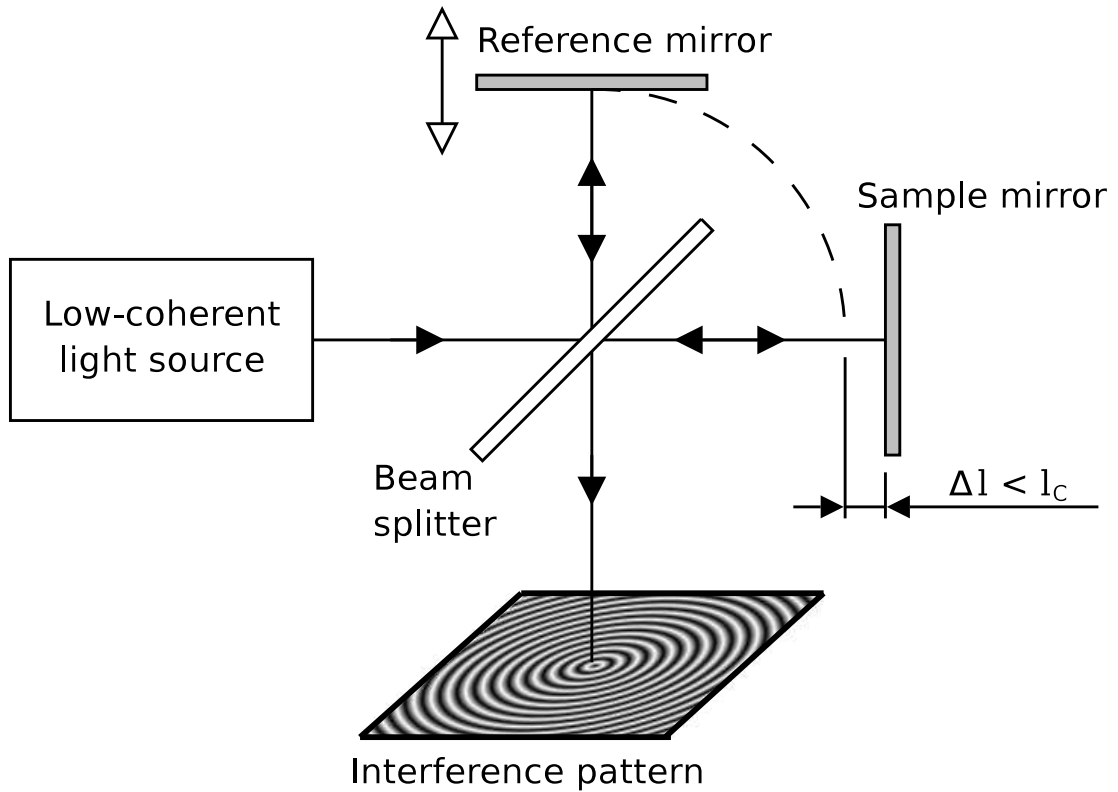
Figure 2.1. Principle of low-coherence interferometry: An interference pattern is present if, and only if, the path difference Δl is smaller than the coherence length l_C of the source.

In optical coherence tomography, only this interference signal is of interest, and the unwanted background light is suppressed by filtering[6]. The light source has a very short coherence length so that only backscattered light from within a thin slice of the sample can generate a signal. Through varying the path length of the reference beam, the depth of the signal's origin in the sample can be changed, and so an axial scan is performed.

2.2. A mathematical view of OCT

The light emitted by the light source is split in the beam splitter into a reference and a sample beam. After reflection, the two electrical fields $E_R(t)$ and $E_S(t)$ from the reference and the sample arm, respectively, are recombined in the interferometer. At its exit appears the electrical field $E_E(t, \Delta t) = E_R(t) + E_S(t + \Delta t)$, which is the sum of the two electrical fields with a time delay $\Delta t = \Delta z/c$ due to the path difference Δz[7]. c denotes the speed of light.

The instantaneous intensity $I(t, \Delta t)$ at the interferometer exit is proportional to the square of the electrical field[5]. ξ is used as a factor to convert between the quantities.

$$I(t, \Delta t) = \xi E_E^*(t, \Delta t) E_E(t, \Delta t) \tag{2.1}$$

A detector measures the time-averaged intensity $\overline{I}(\Delta t)$[7]

$$\begin{aligned}
\overline{I}(\Delta t) &= \langle I(t, \Delta t) \rangle = \xi \langle E_E^*(t) E_E(t) \rangle \\
&= \xi \langle [E_R(t) + E_S(t + \Delta t)]^* [E_R(t) + E_S(t + \Delta t)] \rangle \\
&= \xi \langle E_R^*(t) E_R(t) \rangle + \xi \langle E_S^*(t + \Delta t) E_S(t + \Delta t) \rangle \\
&\quad + 2\xi \, \mathcal{R}\{ \langle E_R^*(t) E_S(t + \Delta t) \rangle \} \\
&= \langle I_R(t) \rangle + \langle I_S(t + \Delta t) \rangle + 2\xi \mathcal{R}\{ \langle E_R^*(t) E_S(t + \Delta t) \rangle \}
\end{aligned} \tag{2.2}$$

The reference intensity $I_R(t)$ stays constant, and the sample intensity $I_S(t + \Delta t)$ will vary slowly with changes in the path length[8]. The information is contained in the cross-spectral term $E_R(t)^* E_S(t + \Delta t)$[6]. The slowly varying parts can be filtered out using a high-pass filter and will be neglected in the analysis.

If only stationary waves are considered[7], the fields can be shifted in time arbitrarily. Therefore, only the time delay Δt is of importance. The relationship between the fields is expressed in terms of the mutual coherence function Γ_{RS}[9].

$$\Gamma_{RS}(\Delta t) = \langle E_R^*(t) E_S(t + \Delta t) \rangle \tag{2.3}$$

This leads to the final expression for the intensity

$$\overline{I}(\Delta t) = 2\xi \mathcal{R}\{ \Gamma_{RS}(\Delta t) \} \tag{2.4}$$

As done commonly, a light source with a Gaussian power spectrum $S_{\mathrm{src}}(\omega)$ is assumed[5, 6, 7, 8]. S_0 is a scaling factor, ω_0 denominates the source's centre frequency and σ_ω its standard deviation.

$$S_{\mathrm{src}}(\omega) = S_0 \exp\left[-\frac{1}{2}\frac{(\omega - \omega_0)^2}{\sigma_\omega^2}\right] \tag{2.5}$$

In practical applications, it is more convenient to deal with the full-width at half-maximum (FWHM) bandwidth $\Delta\omega = \sqrt{8\ln 2}\,\sigma_\omega$ than with the standard deviation[6]. The power spectrum can be rewritten as

$$S_{\mathrm{src}}(\omega) = S_0 \exp\left[-4\ln 2\,\frac{(\omega - \omega_0)^2}{\Delta\omega^2}\right] \tag{2.6}$$

Parseval's theorem states that the autocorrelation $\Gamma_{\mathrm{src}}(\Delta t)$ and the power spectrum $S_{\mathrm{src}}(\omega)$ are Fourier transform pairs.

$$\Gamma_{\mathrm{src}}(\Delta t) = \langle E_{\mathrm{src}}^*(t) E_{\mathrm{src}}(t + \Delta t)\rangle = \mathcal{F}^{-1}\{S_{\mathrm{src}}(\omega)\} \tag{2.7}$$

Fuji et. al. showed[10] that the mutual coherence function $\Gamma_{RS}(\Delta t)$ can be seen as the result of the convolution of the autocorrelation $\Gamma_{\mathrm{src}}(\Delta t)$ with the response function of the sample $h(t)$ if we can assume a linear system.

$$\Gamma_{RS}(\Delta t) = \Gamma_{\mathrm{src}}(\Delta t) * h(\Delta t) \tag{2.8}$$

To calculate the point-spread function, an ideal reflector is assumed in the sample arm so that $h(t) = \delta(t)$. The cross-correlation is then the Fourier back transform of the power spectrum[7]

$$\begin{aligned}\Gamma_{RS}(\Delta t) &= \mathcal{F}^{-1}\{S_{\mathrm{src}}(\omega)\}\\ &\propto \exp\left(-\frac{\Delta\omega^2}{16\ln 2}\Delta t^2\right)\exp(i\omega_0\Delta t)\end{aligned} \tag{2.9}$$

Introducing the path difference $\Delta z = c\,\Delta t$, the equation becomes

$$\Gamma_{RS}(\Delta z) \propto \exp\left[-\frac{1}{\ln 2}\left(\frac{\Delta\omega\,\Delta z}{4c}\right)^2\right]\exp\left(i\omega_0\frac{\Delta z}{c}\right) \tag{2.10}$$

It is more convenient to speak in terms of the centre wavelength λ_0 and the FWHM spectral bandwidth $\Delta\lambda$ instead of the centre frequency ω_0 and the FWHM bandwidth $\Delta\omega$. They are related through

$$\lambda_0 = \frac{2\pi c}{\omega_0} \tag{2.11a}$$

$$\Delta\lambda = \lambda_2 - \lambda_1 = 2\pi c \left(\frac{1}{\omega_1} - \frac{1}{\omega_2} \right) = 2\pi c \frac{\Delta\omega}{\omega_1 \omega_2} \approx 2\pi c \frac{\Delta\omega}{\omega_0^2} \tag{2.11b}$$

where the approximation is valid if the bandwidth is small compared to the centre frequency.

Joining these two equations, the full-width at half maximum of eq. (2.10) is

$$\Delta z_{\text{FWHM}} = \frac{8 \ln 2 \, c}{\Delta\omega} = \frac{4 \ln 2}{\pi} \frac{\lambda_0^2}{\Delta\lambda} \tag{2.12}$$

This is basically equivalent to the coherence length of the light source, but since light has to travel the path twice, the round trip coherence length l_C is used as a measure of depth resolution in OCT[7]

$$l_C = \frac{\Delta z_{\text{FWHM}}}{2} = \frac{2 \ln 2}{\pi} \frac{\lambda_0^2}{\Delta\lambda} \tag{2.13}$$

The photo current $i_P(\Delta z)$ measured by the receiver is proportional to the intensity on the photo diode[7]. Using eq. (2.4) and $\Delta z = c \, \Delta t$ one obtains

$$i_P(\Delta z) \propto \overline{I}(\Delta z) = 2\xi \mathcal{R}\{\Gamma_{RS}(\Delta z)\} \tag{2.14}$$

The path difference Δz is evoked by the movement of the mirror in the reference arm. Assuming a constant motor speed v_M and regarding that the light has to travel the way twice, one gets

$$\Delta z = 2 v_M t \tag{2.15}$$

which can be inserted together with eq. (2.11) into eq. (2.14) to map the photo current to the time domain

$$i_P(t) \propto 2\xi \exp\left[-\frac{1}{\ln 2} \left(\frac{\pi v_M \Delta\lambda}{\lambda_0^2} t \right)^2 \right] \cos\left(i \frac{4\pi v_M}{\lambda_0} t \right) \tag{2.16}$$

This is a high-frequency cosine modulated by a Gauss function. The cosine has an electrical centre frequency f_0 of

$$f_0 = \frac{2v_M}{\lambda_0} \tag{2.17}$$

and after Fourier transforming the photo current, it is obvious that the FWHM electrical bandwidth Δf is equal to

$$\Delta f = \frac{2v_M \Delta \lambda}{\lambda_0^2} \tag{2.18}$$

2.3. Optical properties of tissue

When light hits tissue, its behaviour is often described using characteristic properties like

- index of refraction n,

- scattering coefficient μ_s,

- absorption coefficient μ_a,

- scattering phase function $p(\Theta)$,

- anisotropy factor g and

- reduced scattering coefficient μ_s'.

The index of refraction n is the ratio between the speed of light in vacuum and its phase velocity in the respective medium $n = c/v_{ph}$[11]. According to Mobley and Vo-Dinh, most tissues have a refractive index that is similar to that of water ($n = 1.33$). For lumped tissues it lies in the range from $n = 1.36$ to $n = 1.38$.

Absorption of light takes places in the presence of special molecules called chromophores. The energy can be assimilated by them during electronic, vibrational or rotational transitions[11]. The efficiency of chromophores is given by the absorption coefficient μ_a, and $\exp(-\mu_a L)$ gives the probability that a photon will survive travelling a path of length L through the tissue[12]. The inverse of the absorption coefficient μ_a^{-1} is called absorption mean free path and represents the average length a photon can travel without being absorbed.

Absorption is a highly wavelength-dependent property. In the therapeutic window from 600–1 300 nm, most tissues are sufficiently weak absorbers and allow light to

penetrate[11]. The lower boundary is made up by oxygenated and deoxygenated hemoglobin, the upper dominated by water.

Fluctuations in the index of refraction in the medium, e.g. due to particles of another material, causes scattering. This the part of the incident light being deflected from its original trajectory[13]. Analogous to the absorption coefficient, the probability that a photon can travel a length L without being scattered is $\exp(-\mu_s L)$ with μ_s being the scattering coefficient[11]. The scattering mean free path μ_s^{-1} is the average distance a photon can travel between two scattering events.

Scattering is of interest in diagnostic and therapeutic applications in general[11] and in OCT in particular, as only the light that is scattered back from the tissue to the beam splitter contributes to the signal.

The scattering phase function $p(\Theta)$ is a measure for the angular distribution of scattered photons[14]. To be more precise, it is the probability that a scattered photon will be redirected into a unit solid angle orientated at an angle of Θ relative to its original course.

The anisotropy g, has a close relationship to the scattering phase function. It is the average value of the cosine of the scattering angle, $g = \langle \cos \Theta \rangle$[15], and it applies that $-1 \leq g \leq 1$. If the medium is isotropic, the photons will be scattered in all directions with the same probability, and the anisotropy will be $g = 0$. It will be positive if it is more likely for a photon to be forward scattered than backward.

Biological material is normally highly forward scattering. Common values for the anisotropy are $g \approx 0.9$ for the stratum corneum, $g \approx 0.7$ to 0.8 for the dermis and $g \approx 0.8$ for the epidermis[16].

The reduced scattering coefficient μ_s', can be derived from the scattering coefficient μ_s and the anisotropy g by $\mu_s' = (1-g)\mu_s$. It maps the anisotropic scattering with μ_s and g to an isotropic scattering with a lower scattering coefficient μ_s'[11].

Chapter 3.

Method

This chapter reasons about different topologies of time domain optical coherence tomographs and describes the methods used to evaluate the system.

3.1. System implementation

The implementation of a time domain OCT system with a linear variable delay line was agreed upon. The design would not need a spectrometer as it is necessary for a Fourier domain OCT[7]. Furthermore, the electrical frequency of the measured signal could be adjusted by changing the speed of the delay line according to eq. (2.17).

The interferometer could be implemented in different topologies e. g. as a standard Michelson interferometer (fig. 3.2 on page 13), a power-conserving Michelson interferometer or a Mach-Zehnder interferometer (fig. 3.1 on page 12)[17]. The Mach-Zehnder interferometer and the Michelson interferometer in its power-conserving configuration had the advantage that they were energy efficient because all of the backscattered light was fed to a detector. In the normal Michelson interferometer configuration, one half of the backscattered light was led back to the light source and lost, therefore. However, it needed neither balanced detection nor an optical circulator, and it was easier to align as just two fibre lengths had to be matched. Thus the standard Michelson interferometer was preferred.

One more choice had to be made on the implementation of the interferometer beside its topology. It could either be set up with free-space optics or with fibre optics. Although the fibre based version brought some complications along, like the matching of the fibre lengths, for example, it seemed more robust than the free-space optics and was probably less complicated to align.
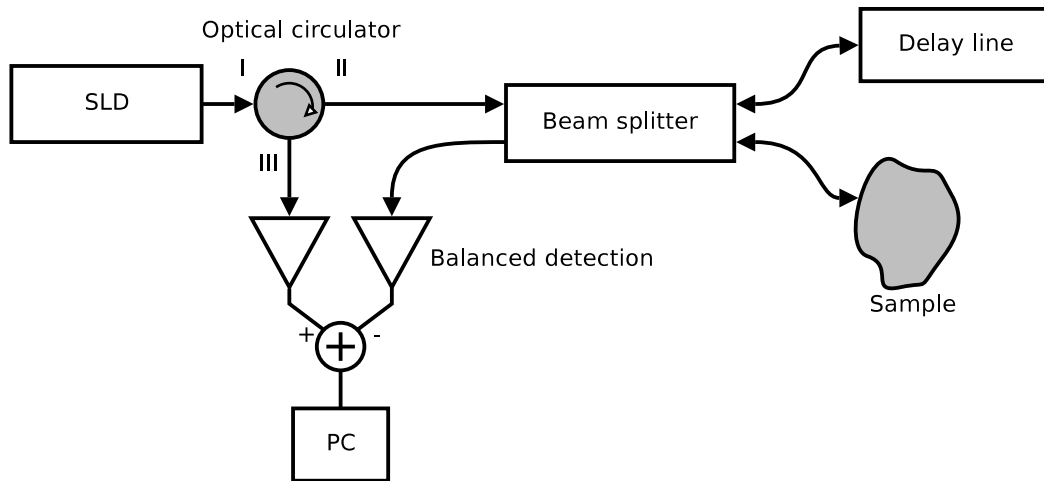
(a) Power-conserving Michelson interferometer
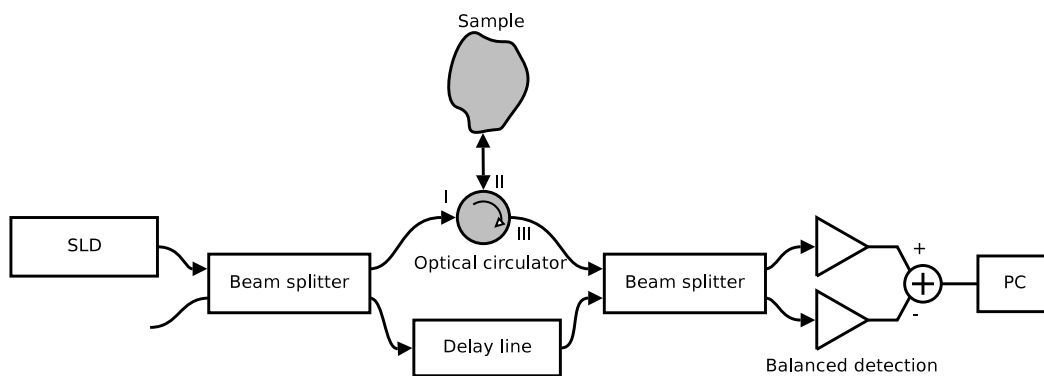
(b) Mach-Zehnder interferometer

Figure 3.1. Two types of power-conserving interferometer configurations for optical coherence tomography (from[17])
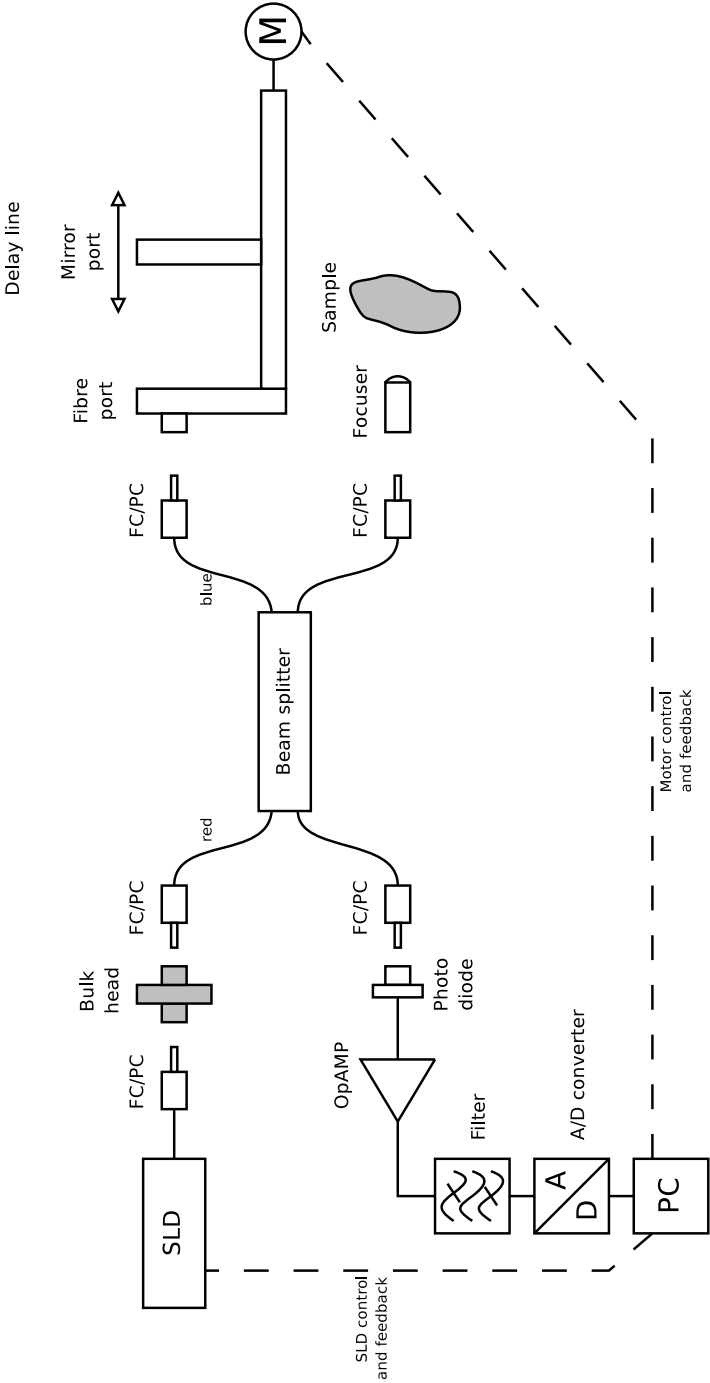
Figure 3.2. Implemented OCT system

Finally, an OCT system using a fibre based Michelson interferometer was implemented. The whole system was made up of four independent sub-systems that could be easily connected together using the fibre beam splitter. Those parts were a super-luminescent diode (SLD), a variable optical delay line, a sample focuser and a detection circuit. They can be seen together with their interconnections in figure 3.2.

3.2. System evaluation

Basic tests were made to evaluate the implemented system. They are described in the following.

3.2.1. Verification of the signal origin

To prove that the signal indeed stems from the object in the sample arm and is not some kind of artefact, a mirror in the sample arm was scanned in three fixed positions along the z-axis with a shift of approximately 100 µm from scan to scan. The measurements should look the same except for a shift in the z-direction.

3.2.2. Repeatability

Referring to the OCT system, the repeatability is the variation of the depth measurement if the same object in the same position is measured multiple times[18].

To determine the repeatability, a mirror was measured 100 times and the position of the signal's peak was extracted from each measurement. The peak should be located at the same depth for every scan.

3.2.3. Signal-to-noise ratio

To determine the order of magnitude of the system noise, a mirror located nearly at the working distance of the lens was measured. The maximum value from the mirror was taken as the signal intensity I_{signal} and the mean value of the rest of

the signal as the noise intensity I_{noise}. The signal-to-noise ratio (SNR) in dB was calculated according to

$$\text{SNR} = 10 \log \left(\frac{I_{\text{signal}}}{I_{\text{noise}}} \right) \tag{3.1}$$

Chapter 4.

Material

In the following chapter, the material used in the project is listed. It starts with the software necessary for controlling the hardware and doing the data processing, continues with the system's hardware and finishes with the phantoms needed for the evaluation process.

4.1. Software

To control the system from the PC, mainly the graphical programming language LabVIEW™ 6.1 (National Instruments Corporation, Austin, USA) was used. Time critical parts were written in Visual C++® 6.0 (Microsoft Corporation, Redmond, USA) and exported as a DLL to LabVIEW. The signal processing part was done in MATLAB® 6.5 (The Mathworks, Inc., Natick, USA). The circuit diagrams and layouts were drawn in EAGLE™ 4.14 Light (CadSoft Computer GmbH, Pleiskirchen, Germany).

4.2. Beam splitter

The beam splitter C-WD-AL-50-H-2210-35-NC/NC (Laser 2000 AB, Norrköping, Sweden) was chosen as an interface between the different entities of the OCT system and used to divide the light into two rays for the sample and the reference arm, respectively. It was made of a single mode fibre suitable for 1 300 nm with a core diameter of 9 µm and had a coupling ratio of nearly 50 %. A single mode fibre was selected because of its lower dispersion compared to a multi mode fibre[19]. The beam splitter's properties can be found in table 4.1.

Fibre type	SMF-28
Core diameter	9 µm
Operating wavelength	1 310/1 550 nm
Bandwidth	±40 nm
Coupling ratio	49.2 %
Insertion loss	3.32 dB
Polarisation dependent loss	< 0.1 dB
Directivity	60 dB
Return loss	55 dB

Table 4.1. Characteristics of the beam splitter

Together with the choice of the beam splitter, a second choice of the fibre's connectors had to be made. For single mode fibres several different connectors may be used, whereof FC/PC (Fibre Connector/Physical Contact) and FC/APC (Angled Physical Contact) are two common possibilities. The latter has a surface that is polished on an 8° angle, which reduces the amount of reflected light[20].

The selected super-luminescent diode was already pigtailed with a FC/PC connector. Therefore, the same connector was chosen throughout the system. This avoided possible problems due to interchanged connectors.

As shown in figure 4.1, the lengths of the reference (blue) and the sample arm (white, right side) differed by 13.7 mm which introduced a difference in the time-of-flight between the two beams. However, it was possible to compensate for this with the help of the delay line. Thus it was not necessary to adapt the fibre lengths.

To connect the beam splitter to the diode an additional bulk head 110-301-904V002 (Laser 2000) with two FC/PC receptacles was needed. All other parts could be connected to the splitter directly since they were already equipped with FC/PC receptacles.

4.3. Super-luminescent diode

The light source had to be chosen carefully, as the wavelength played an important role. First, it had to lie within the therapeutic window, which ranges from 600–1 300 nm, to make measurements on tissue possible. Second, it determined, together with the source's bandwidth, the achievable axial resolution as stated in eq. (2.13).
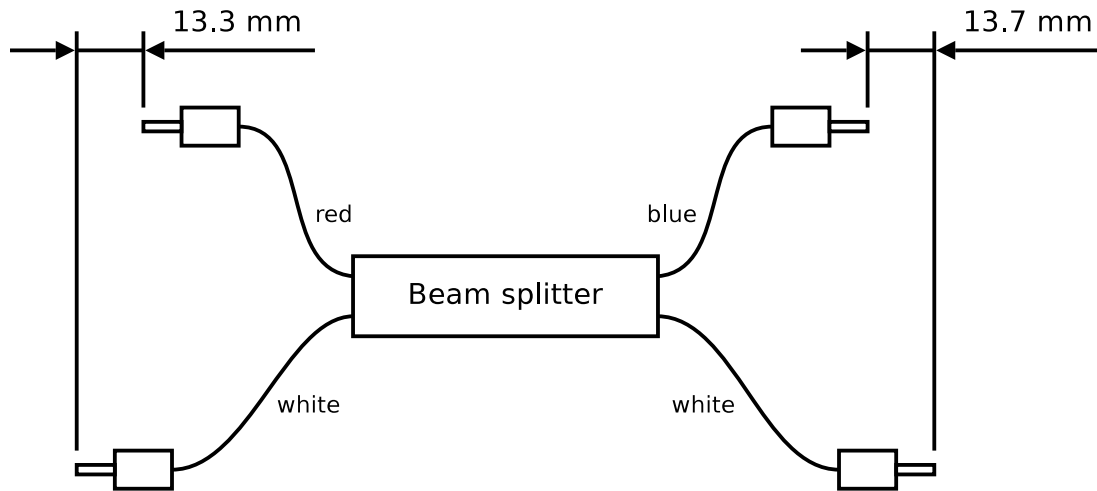
Figure 4.1. Length differences of the beam splitter fibres

The choice was a super-luminescent diode (SLD) mounted on an evaluation board (Kamelian Ltd., Glasgow, UK) with a centre wavelength in the near-infrared. The characteristics of the diode are summarised in table 4.2.

Typical output power	7 mW
Centre wavelength	1 295 nm
FWHM	45 nm

Table 4.2. Technical specification of the SLD

The spectrum of the diode could not be verified as there was no spectrometer for the near-infrared range available. Therefore, the SLD's parameters were taken from the sample spectrum in fig. 4.2. The centre wavelength lay around $\lambda_0 = 1\,295$ nm, and the full-width at half-maximum—or 3 dB—bandwidth was $\Delta\lambda = 45$ nm. Together with eq. 2.13, these values led to an axial resolution of $l_C = 16.4$ nm.

4.3.1. Communication protocol

Unfortunately, it was not possible to get information on the communication protocol between the evaluation board and the PC. The commands were gathered by logging the traffic over the serial port while making different adjustments in Kamelian's own program. A command description can be found in appendix A.
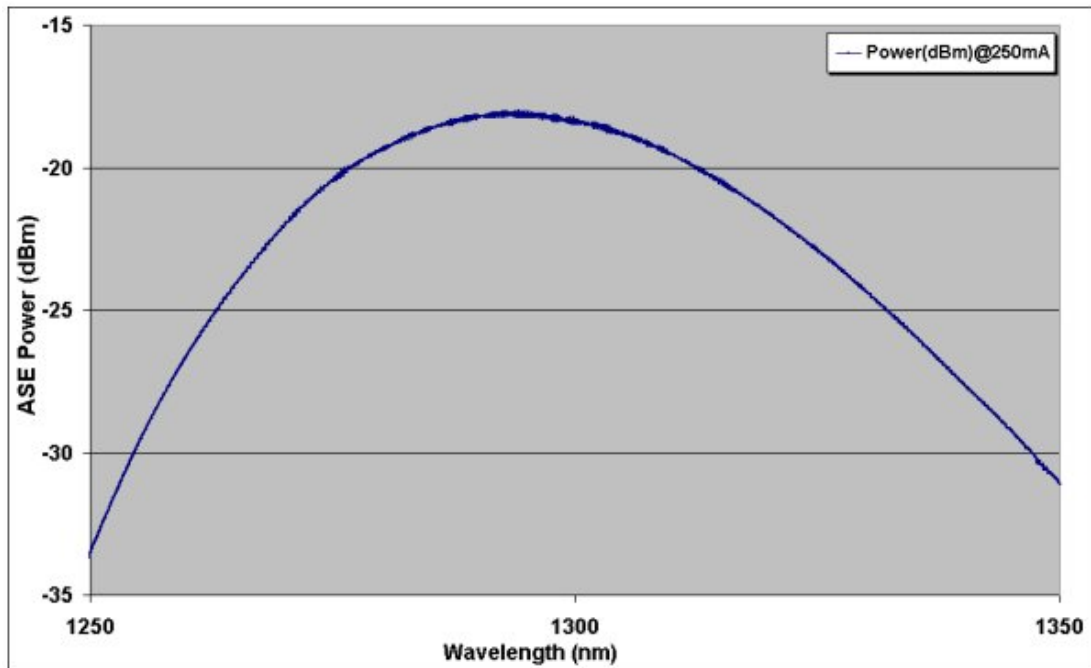
Figure 4.2. Sample spectrum of a Kamelian SLD 1300 nm (from `http://www.kamelian.com/graphs/o_sld_spc.html`)

4.3.2. Initialisation sequence

In fig. 4.3, the initialisation sequence for the SLD evaluation board, as it was used by Kamelian's control software, is shown. To be compatible, all steps except the last one were executed the same way.

First of all a carriage return was sent, to which the board should answer with 'Syntax error'. In the next step the board's identification string 'Kamelian OPA Controller 1.13' was read. The meaning of the following three commands was unfortunately unknown: First the parameter 43 was read, and the result was ignored. Next the return value of the setting 102 should be '001' and of the setting 8 '008'. Then the 32 data strings of the board's data block were acquired, and after that the parameter 52 was queried whose result was again thrown away. The board was set to constant current mode, and the current was set to 10 mA. The last step differed from the original initialisation sequence, where the current was set to 100 mA. The lower value was chosen for safety reasons.

Figure 4.3. Initialisation of the SLD evaluation board

4.3.3. Thermoelectric cooling

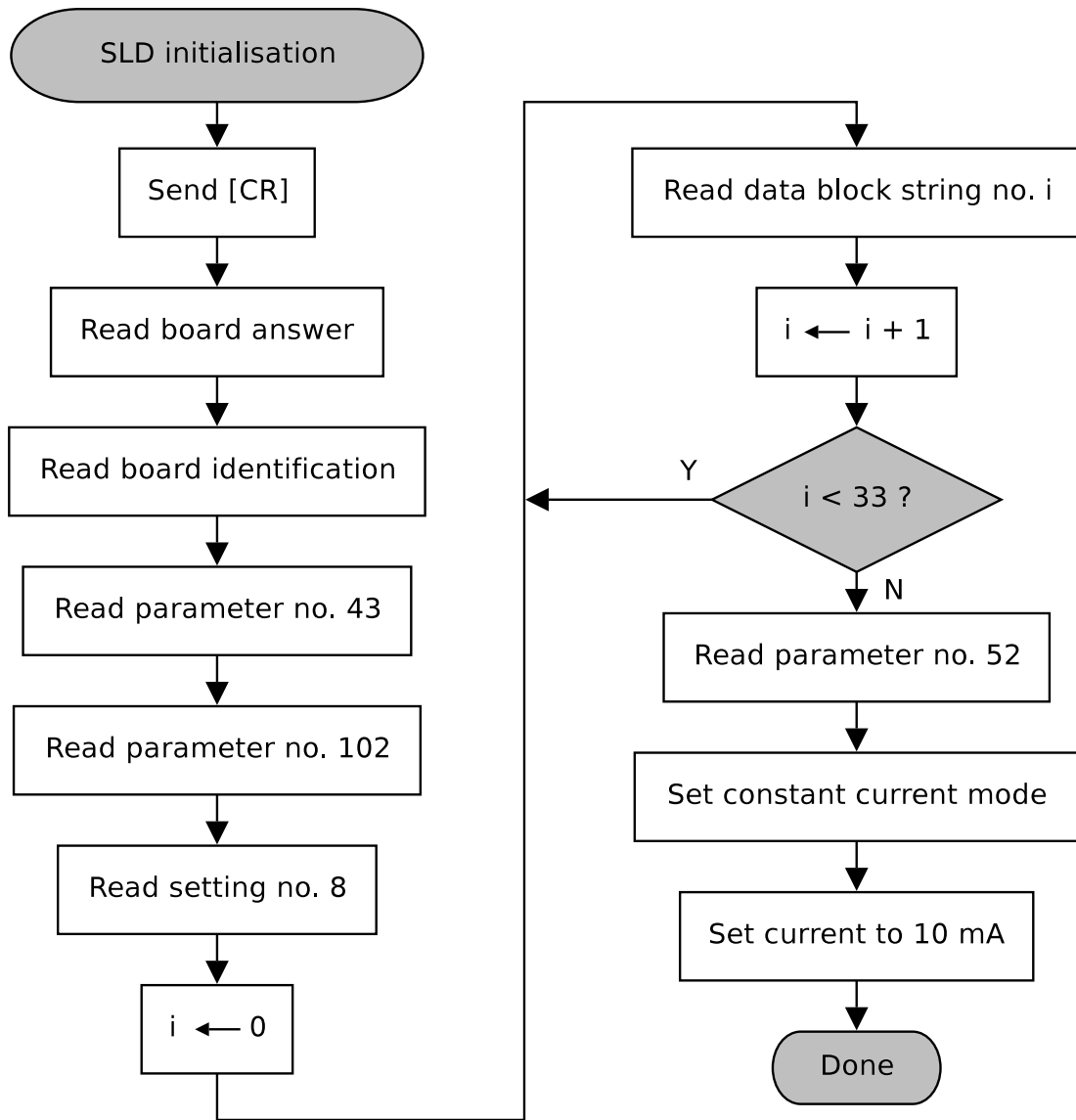The SLD should also provide a built-in cooling system, but it regrettably was not working. So the board was cooled down using an external Peltier element, which was powered by a constant current of 1.5 A and controlled by the PC. The supply current was switched off and on, whenever the temperature of the SLD left the software tunable hysteresis around the desired set point. A schematic of the control circuit for the TEC is show in appendix F in fig. F.4.

4.4. Delay line

The delay line consisted of the following parts:

- Fibre bench FB-VDL-25 (OFR Inc., Caldwell, USA)

- Fibre port PAF-X-5-1310 (OFR)

- Mirror port FMB-1310 (OFR)

- DC motor EncoderDriver 10 mm (37-0494) (Ealing Catalog Inc., Rocklin, USA)

The fibre bench provided a mean to mount the fibre port as well as the mirror port. The distance between them could be varied within 25 mm. This was accomplished using the DC motor which itself was controlled by a PC. The fibre port had a built-in collimator that produced a parallel beam with a diameter of 1 mm. This ray was reflected by the mirror port and collected by the fibre port again, which refocused the light back into the fibre. A short instruction on how to align the delay line can be found in appendix B.

4.4.1. DC motor

Table 4.3 lists the specification of the DC motor used in the system

Maximum travel	10 mm
Lead screw pitch	0.7 mm
Encoder counts per mm of travel	3 666
Approximate speed	0.6 mm/s

Table 4.3. Characteristics of the DC motor

An H-bridge circuit TPIC0107B (Texas Instruments Inc., Dallas, USA) was used to control the DC motor. The bridge itself was controlled by the PC via a DAQCard-700 (National Instruments). The two input signals for the H-bridge, PWM and DIR, were connected to the DAQ-pins DOUT0 and DOUT1, respectively. The following table shows the possible states of the digital output lines and the corresponding motor movement. The positive direction was defined by a counterclockwise rotation of the spindle which means that it moved out of the motor chassis.

DOUT1 (DIR)	DOUT0 (PWM)	Spindle movement
0	0	none
0	1	negative
1	0	none
1	1	positive

Table 4.4. Direction of motor movement

The DC motor provided two phase shifted quadrature signals to track the movement. The amount of pulses from each sensor was determined to be 3 666 per millimetre of travel. Encoder channel B was connected to counter 1 of the DAQCard-700 to count the number of steps moved and calculate the travel distance, respectively.

Controlling the motor

In fig. 4.4, the motor's answer to the step function can be seen. Counter 1 was initialised to $n = 1\,000$, the desired amount of steps to move. At $t = 0\,\mathrm{s}$ the motor was switched on. Approximately $150\,\mathrm{ms}$ after the start-up, it was running with a constant speed. As soon as the counter reached zero, the motor was switched off, but due to its inertia it still continued to rotate for another 264 steps.

To overcome this problem of inexact positioning, a C++ DLL was written which provided the function `moveMotor` to drive the motor using pulse width modulation (PWM). The processor clocks served as a high-resolution timer to generate the PWM signal[21].

First, the motor was driven with a duty cycle of $100\,\%$. If only 500 pulses were left, the regulation started. The duty cycle was decreased so that no encoder pulse arrived for a time of 10^7 processor clocks. Hereafter it was increased steadily until the motor rotated one step and decreased immediately again. This procedure kept the motor always between a resting state and a slow motion involving a low inertia. See fig. 4.5 on page 25 for a flowchart of the function.
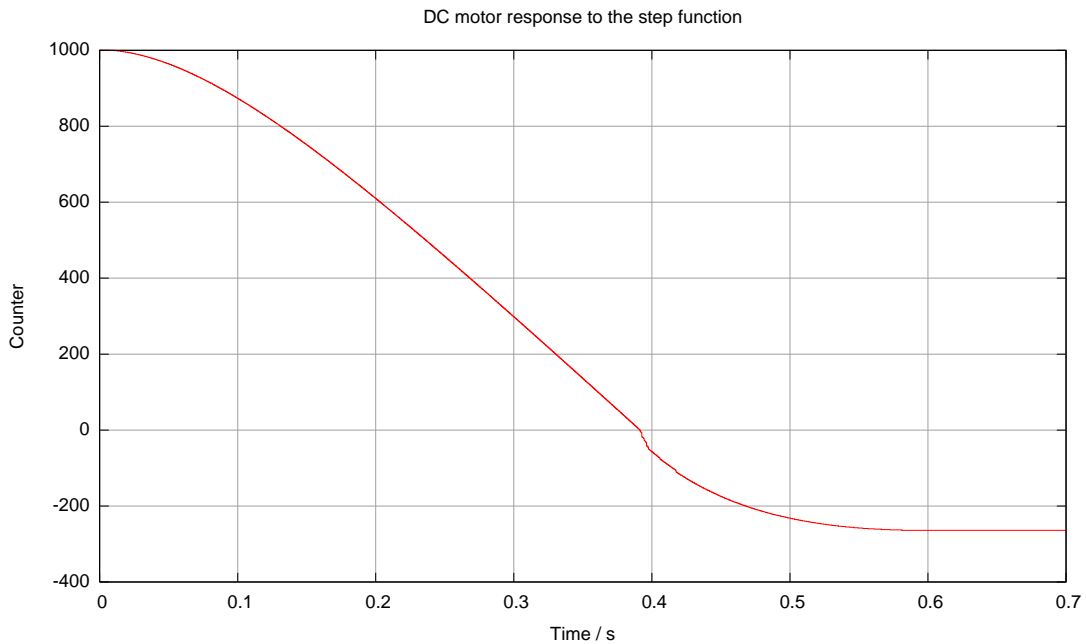
Figure 4.4. Step response of the DC motor

The motor speed was not predictable during start-up (fig. 4.4) and so the OCT signal, which is connected to the motor speed via eq. (2.17), could not be predicted. It was preferable to cast away approximately 300 steps after the motor start and just take the linear part. The program provided the parameter *scan extend* which contained the amounts of steps to be sampled before and after the actual measurement range.

4.5. Detection and analogous signal processing

The analogous signal processing chain can be broken down into five parts: a photo diode to convert the light into a current, a transimpedance amplifier to convert the photo current into a voltage, a band-pass filter to reduce noise and remove the unwanted background intensity, an adjustable voltage amplifier to utilise the full dynamic range of the analogue-to-digital converter and the A/D transducer.

An InGaAs photo diode NT55-756 (Edmund Optics Inc., Barrington, USA) was used to measure the output of the beam splitter fibre. It was already mounted in a FC/PC receptacle which matches the connectorised beam splitter connector.
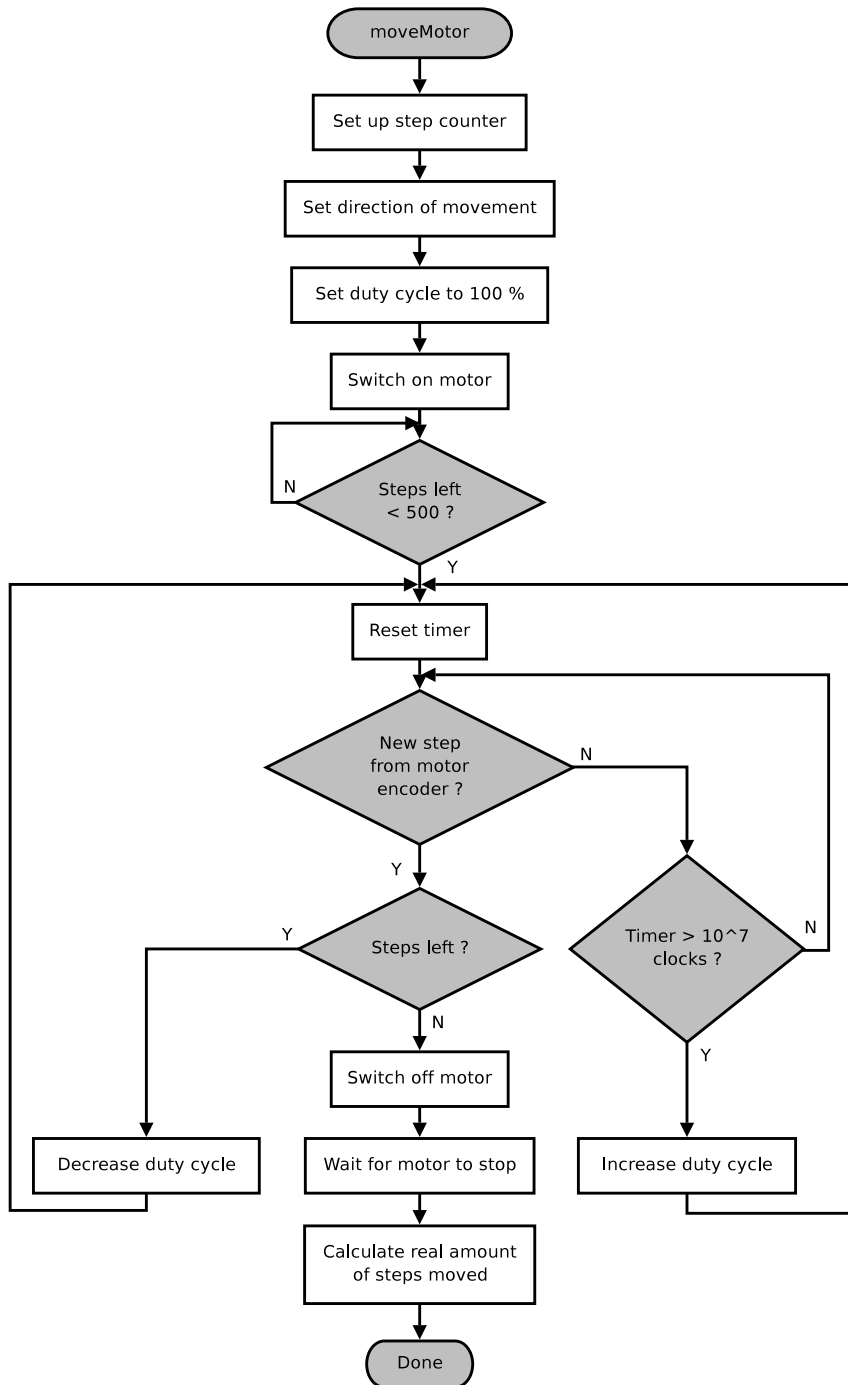
Figure 4.5. Controlling the DC motor by pulse width modulation

Due to the small sensing area with a diameter of 70 µm, the diode's parasitic capacitance was small, too. The responsivity reached up to 0.9 A/W at 1 310 nm. The maximum backward current was limited to 1 mA, which leads to a maximum measurable optical power of $P_{max} = \frac{1\,\text{mA}}{0.9\,\text{A/W}} \approx 1.11\,\text{mW}$. Table 4.5 summarises the important properties.

Sensing area diameter	70 µm
Minimum responsivity at 1 310 nm	0.85 A/W
Maximum responsivity at 1 310 nm	0.9 A/W
Capacitance	0.65 pF
Maximum reverse current	1 mA
Typical dark current	30 pA
Maximum dark current	3 nA

Table 4.5. Technical specification of the photo diode

A photo diode is usually driven either in the third or in the fourth quadrant of the current-voltage characteristic, which is called photo conductive or biased mode (figure 4.6(a)) and photo voltaic mode or unbiased mode (figure 4.6(b)), respectively[22]. A highly-linear response to the incident illumination could be achieved by operating in unbiased mode with zero load, through feeding the detector output to the virtual earth of the transimpedance amplifier IC_1 (see fig. 4.7 on page 28). It's feedback resistor R_1 is dimensioned to produce an output voltage of 4.7 V if the input current is 1 mA.

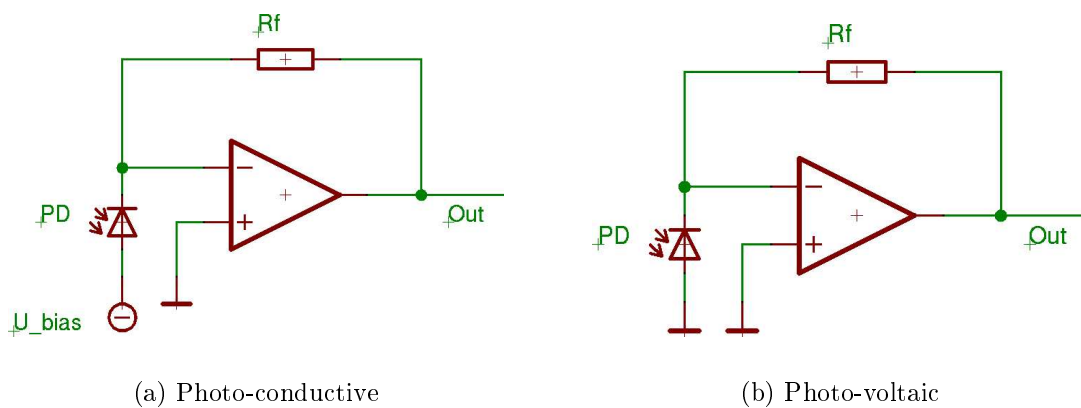(a) Photo-conductive   (b) Photo-voltaic

Figure 4.6. Modes of operation of a photo diode

The band-pass filter (also fig. 4.7) in turn was made up of a low-pass and a high-pass filter. Each one was a second order filter implemented in Sallen-Key topology[23].

Eq. (2.17) and (2.18) and the motor speed of $v_M = 0.6\,\mathrm{mm/s}$ (see 4.4.1) yield an electrical centre frequency $f_0 = 927\,\mathrm{Hz}$ and a 3 dB bandwidth $\Delta f = 32\,\mathrm{Hz}$.

IC_2 together with the resistors $R_3 = 6.8\,\mathrm{k\Omega}$ and $R_4 = 12.7\,\mathrm{k\Omega}$ and the capacitors $C_1 = 22\,\mathrm{nF}$ and $C_2 = 10\,\mathrm{nF}$ formed a low-pass with the upper cut-off frequency $f_u \approx 1.15\,\mathrm{kHz}$.

The next stage, IC_3 together with $R_5 = 6\,\mathrm{k\Omega}$, $R_6 = 12\,\mathrm{k\Omega}$ and $C_3 = C_4 = 33\,\mathrm{nF}$, was a high-pass with the lower cut-off frequency $f_l \approx 565\,\mathrm{Hz}$.

As a last measure, the non-inverting amplifier IC_4 could be adjusted by the potentiometer R_7 to increase the signal to the full swing range ($\pm 5\,\mathrm{V}$) of the DAQCard-700's A/D converter.

The filtered and amplified signal was finally sampled by the DAQCard-700 with a sampling frequency of up to 33.3 kHz. At the same time, the two encoder signals from the DC motor (see 4.4.1) were sampled to provide track of the position in the reference arm.

4.6. Sample focuser

The sample focuser was used to focus the light from the beam splitter fibre to a small spot into the tissue and collect the backscattered light and focus it back into the fibre again.

A few constraints were put on the focuser:

- It had to be easily mountable on a FC/PC connector if possible without adapter or additional alignment necessary.

- The numerical aperture (NA) of the focuser at the fibre side should be equal to the one of the single mode fibre to guarantee that the device works well in both directions.

- The NA on the sample side should be large, to collect as much of the reflected light as possible. That requirement however, downgraded the system's performance, as it increased the probability of collecting multiple scattered photons which impair the image quality[24].
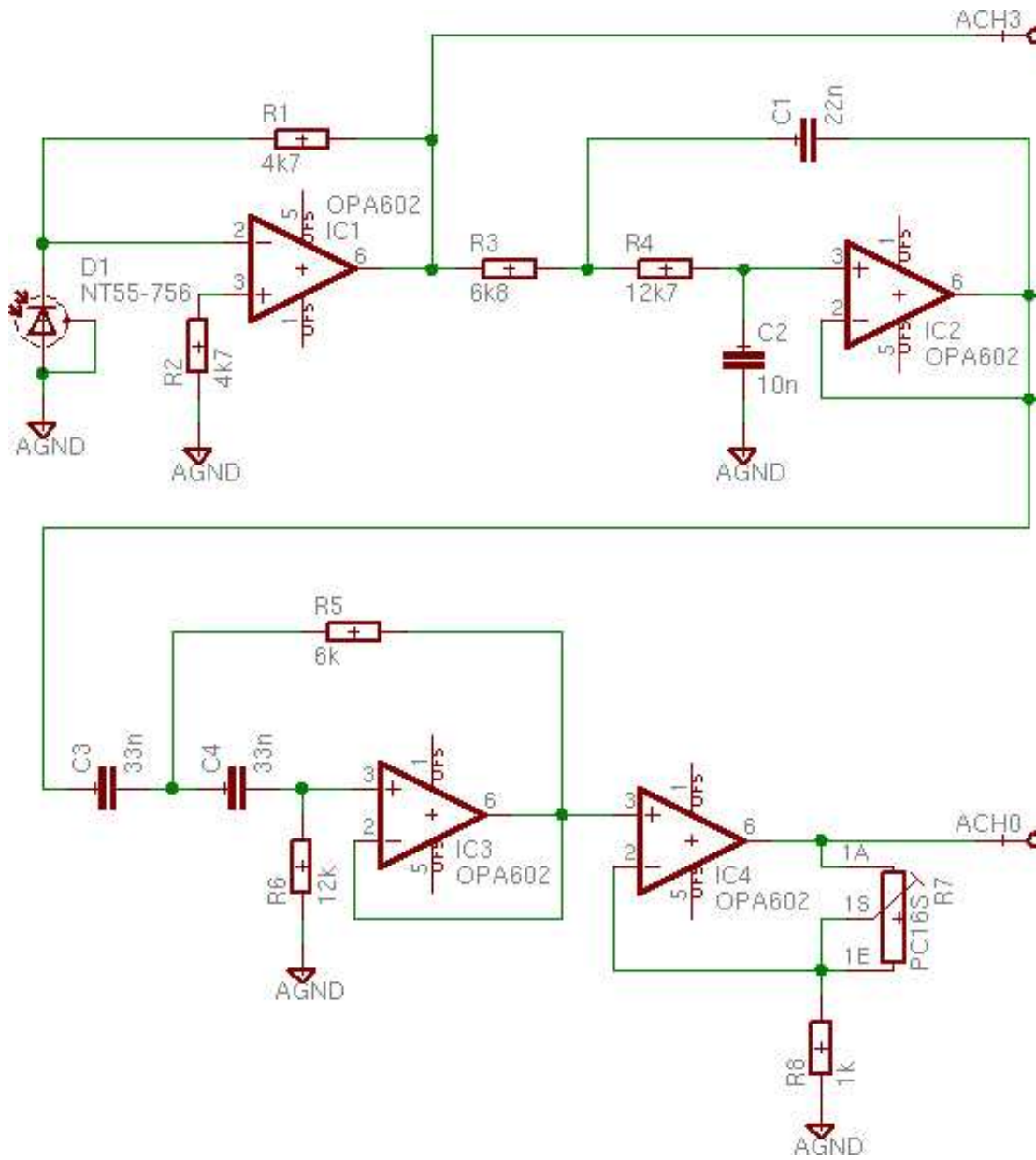
Figure 4.7. Detection circuit

Two different types of focusers were tried during the project. The sleeve type collimator BK-FC4 (OECA GmbH, Dahlwitz-Hoppegarten, Germany) outfitted with a FC/PC receptacle, could be mounted on the beam splitter's FC/PC connector directly. It had a focal spot diameter of less than 20 μm on a length of approximately 100 μm.

Although the focusing of this device was good, it did not work well as a collector. The intensity declined too much as soon as an other object rather than a mirror was used in the sample arm. Probably the numerical aperture at the fibre side was too high so that the injection of light into the fibre was poor.

Therefore, a GRIN rod lens GT-IFRL-100-0017-50-NC together with a connector mount for FC/PC 2.5 mm to 1.0 mm GRIN-lens (GRINTECH GmbH, Jena, Germany) was used. The lens had a working distance of 1.7 mm and a numerical aperture of NA = 0.5.

The lens was mounted on the FC/PC connector of the beam splitter as can be seen in fig. 4.8. A drop of silicon oil (Rhodorsil 47 V 20, SIKEMA AB, Stockholm, Sweden) with a refractive index of $n = 1.4$ was placed between the FC/PC connector and the GRIN rod lens to prevent unwanted reflections because of an air buffer. The oil's adhesive force also held the lens in place.
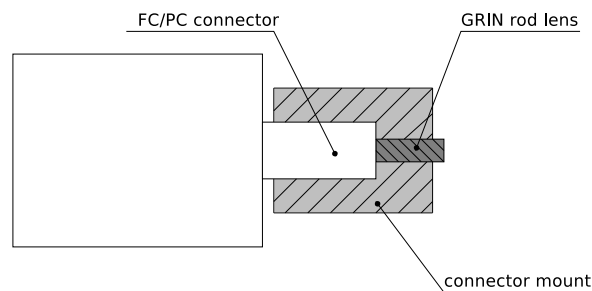

Figure 4.8. Sketch of the mounted GRIN rod lens

For all measurements mentioned in this report, the GRIN rod lens was used as sample focuser.

4.7. Phantoms

Solid phantoms were needed to make the basic tests on the OCT system. Two different types were used in the evaluation process: foil phantoms constructed out of filter foils and gel-like agar phantoms.

4.7.1. Foil phantoms

No.	Name	Thickness µm
#27	Medium Red	63
#47	Light Rose Purple	36
#67	Light Sky Blue	63
#89	Moss Green	36

Table 4.6. Properties of the Roscolux filter foils

The first kind of phantom was made up of Roscolux filter foils (Rosco Laboratories Inc., Stamford, USA). Although the optical properties μ_a and μ_s of those foils were not known, they were quite thin and could be used to test the system resolution. Table 4.6 shows the dimensions of the foils and table 4.7 the stacking sequence. A drop of water between the foils kept them adhered together.

No.	Filter foils (under-most first)
1	#47
2	#27 - #89
3	#27 - #47 - #27 - #47
4	#27 - #89 - #67 - #27 - #89 - #67

Table 4.7. Composition of the foil phantoms

4.7.2. Agar phantoms

Those phantoms were produced according to a project work by Hartleb[25]. A mixture of 0.5 g agar (Difco Agar, granulated, Becton, Dickinson and Company, Sparks, USA) and 44.5 ml deionised water was used as a basis. Ink (Artline xylene free marking ink, ESK-20, black, Shachihata Inc., Malaysia) diluted in

acteone (Gripen Aceton, SC Johnson Scandinavia, Kista, Sweden) was added as an absorber, and Vasolipid (Vasolipid 200 mg/ml B. Braun Medical AB, Bromma, Sweden) acted as scattering additive.

The scattering and absorption coefficients of the final phantoms, μ_s and μ_a, respectively, could be calculated with the next two formulae[25]. C_{ink} is the dimensionless concentration of diluted ink and C_{vaso} is the one of Vasolipid.

$$\mu_a = 2\,500\,\mathrm{cm}^{-1} \cdot C_{ink} \tag{4.1}$$
$$\mu_s = 3\,400\,\mathrm{cm}^{-1} \cdot C_{vaso} \tag{4.2}$$

The substances were mixed so that the scattering coefficient of the phantom matched the reduced scattering coefficient of the tissue, and the absorption coefficients were the same. The values were taken from[11] and can be seen in the next table. They are valid for 633 nm, which is the wavelength Hartleb used for her measurements.

	g	μ_a cm^{-1}	μ_s cm^{-1}	μ_s' cm^{-1}
Epidermis	0.8	35	450	90
Dermis	0.8	2.7	187.5	37.5

Table 4.8. Optical properties of skin layers

Four different kinds of agar blocks were made. The following table lists them together with their properties:

Name	μ_a cm^{-1}	μ_s cm^{-1}	Description
Abs	10	—	Only absorbing
Scat	—	18	Only scattering
Der	2.4	34	Imitates dermis
Epi	32	80	Imitates epidermis

Table 4.9. Properties of the agar blocks

To make thin slices, the blocks were cut with a Vibratome® (Vibratome® Sectioning System Series 1000, Technical Products International Inc., St. Louis, USA) into slices with a thickness down to 200 µm. The slices were stacked to produce the phantoms enumerated in table 4.10. A microscope slide (SuperFrost

Objektträger, MICROM International GmbH, Walldorf, Germany) was used as carrier.

According to Martini[26], the thickness of the whole skin reaches from ca. 1.5 to 4 mm and of the epidermis from ca. 80 to 500 µm. Phantoms no. 3 and 4 were designed to mimic skin tissue.

No.	Slices under-most first, thickness in µm
1	Epi 200 - Der 200 - Epi 200 - Der 200
2	Epi 500 - Der 500 - Epi 500 - Der 500
3	Der 1 000 - Epi 200
4	Der 2 000 - Epi 200
5	Scat 500 - Epi 200 - Scat 500 - Epi 200
6	Scat 500 - Der 200 - Scat 500 - Der 200

Table 4.10. Composition of the agar phantoms

Chapter 5.

Signal processing

The LabVIEW™ program was used to simultaneously sample the two encoder signals from the motor and the detector output. The values were written into a text file and exported to MATLAB®, where all the digital signal processing was done.

5.1. Processing the A-scans

First, the depth information had to be reconstructed from the samples of the motor encoder. The sampled encoder signal was thresholded, and the first differences were calculated to get a Dirac impulse at every signal edge, i.e. at every half of every motor step.

Each edge was assigned to one half of a motor step and the samples in between were linearly interpolated. As the motor's real position is undetermined before and after the last edge, these samples were discarded. The distances could easily be transformed from motor steps to μm as the amount of steps per millimetre was known (see 4.4.1).

The envelope could be generated either by rectification and low-pass filtering[6] or by calculating the absolute value of the analytic continuation[27]. The latter was chosen since it did not require the design of a digital filter and MATLAB® already provided a function to calculate the Hilbert transform $\mathcal{H}$.

According to Granlund[27], the analytic continuation $V(z)$ was obtained from the OCT signal's intensity $I(z)$ via

$$V(z) = I(z) - i\mathcal{H}\{I(z)\} \tag{5.1}$$

and was then used for generating the envelope $\hat{I}(z)$

$$\hat{I}(z) = \sqrt{V^*(z)V(z)} \tag{5.2}$$

5.2. Locating the lens

After the first measurements it was clear that the position of the OCT signal was not stable because of shortcomings in the motor's mechanical guidance (see 6.3). A solution was to align the scans to a reflection from a reference surface that would be sampled in every turn. The lens of the sample focuser was ideal for this task.

The first task was to generate a lens template, i. e. a characteristic pattern that would later be used in the search process. The lens was scanned 100 times. The envelopes were down-sampled to full motor steps, and the cross-correlations between them were calculated. They were brought into line using the maximum of the cross-correlation. After averaging all 100 scans and subtracting the mean value, the lens template, which is shown in fig. 5.1, was obtained.
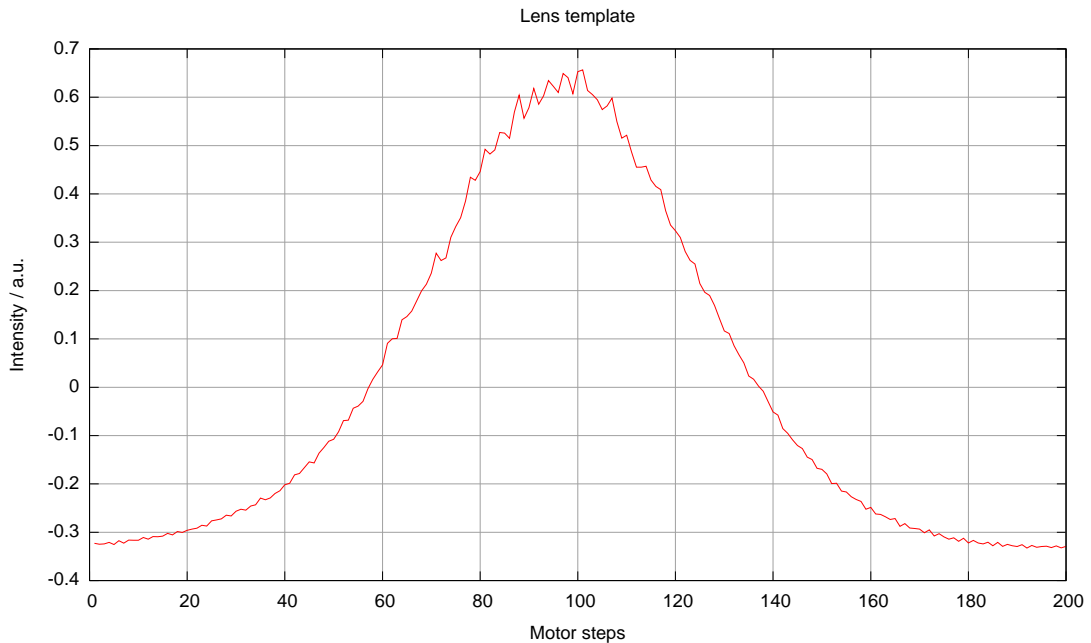

Figure 5.1. Lens template

Before the lens could be searched in the A-scans, they had to be down-sampled to whole motor steps, too. To reduce spikes, they were additionally filtered with a moving median filter with a kernel length of 11 steps.

Next a user-defined part of the first A-scan, which contained the lens, was correlated with the lens template. The lens position was defined as the depth with the best (i.e. the highest) correlation.

It was assumed that the backscattered intensity from the lens would not vary more than $\pm 20\,\%$ in subsequent scans. Thus in the following scan all points were filtered out that had an intensity in the desired range. Furthermore, the one point that was closest to the previous lens position was located. Within a window of ± 2 template lengths around that point, the algorithm looked for a new correlation maximum which defined the lens position of that scan.

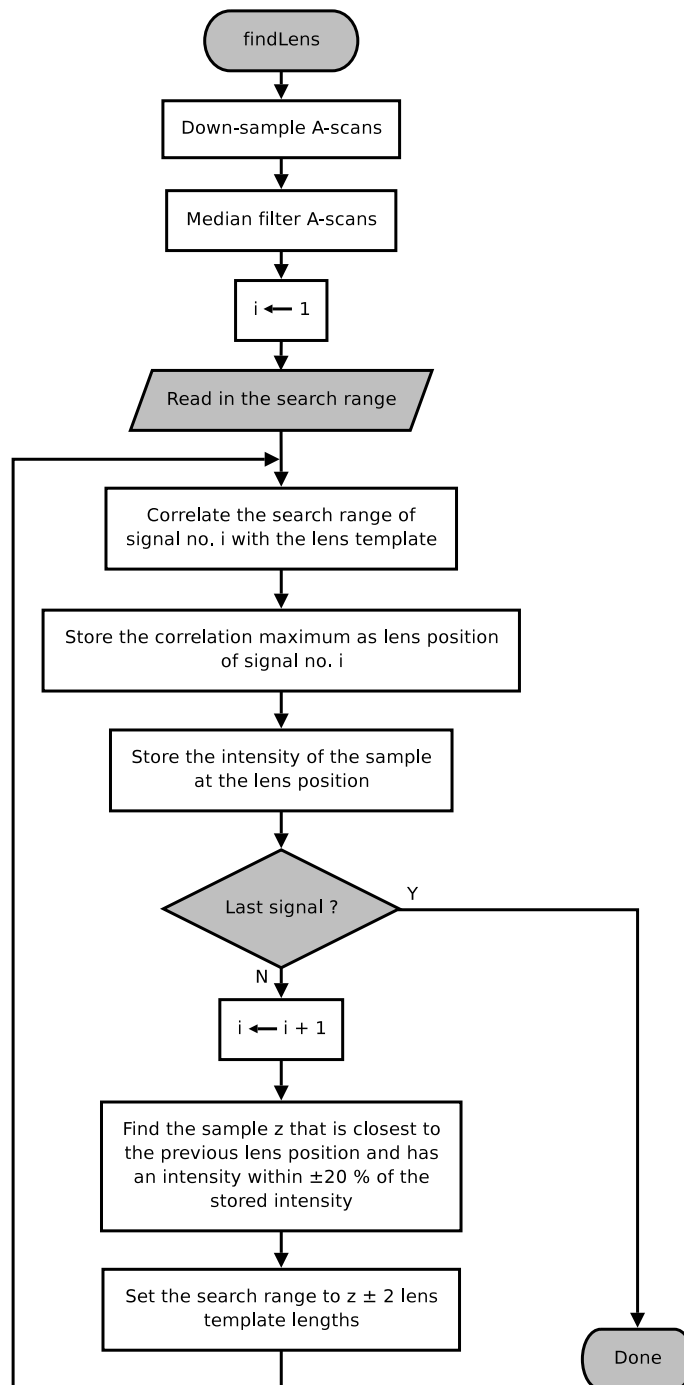Having determined the lens's position in every scan, they could be aligned easily by just shifting the z-axis.

Figure 5.2. Algorithm to locate the lens

Chapter 6.

Results

This chapter contains the results of the project work. First the characteristics of the OCT signal itself will be described, next follows a part about the system parameters, and afterwards the results of the measurements on the phantoms will be presented.

6.1. OCT signal

Fig. 6.1 on page 38 shows the OCT signal from a mirror in the sample arm. The intensity measured with the photo diode is plotted versus the delay line's motor position. It can be seen that it consists of a high-frequency cosine modulated by a Gauss function as predicted in 2.2. The FWHM of the OCT signal's envelope is $15\,\mu m$.

As the amplification can be varied through the operational amplifier IC_4 (see section 4.5), there is no fixed relationship between the measured values and the optical power anymore. Therefore, the intensity is given in arbitrary units (a. u.).

The motor position's origin can be chosen arbitrarily. The depth is thus only a relative measure and is not connected to the distance to the fibre focuser or something similar.

6.2. Verification of the signal origin

The mirror in the sample arm was scanned three times in different positions. Fig. 6.2 shows that the maxima of the OCT signals lie at $136\,\mu m$, $226\,\mu m$ and $319\,\mu m$, which proves that the mirror is the source of the OCT signal.
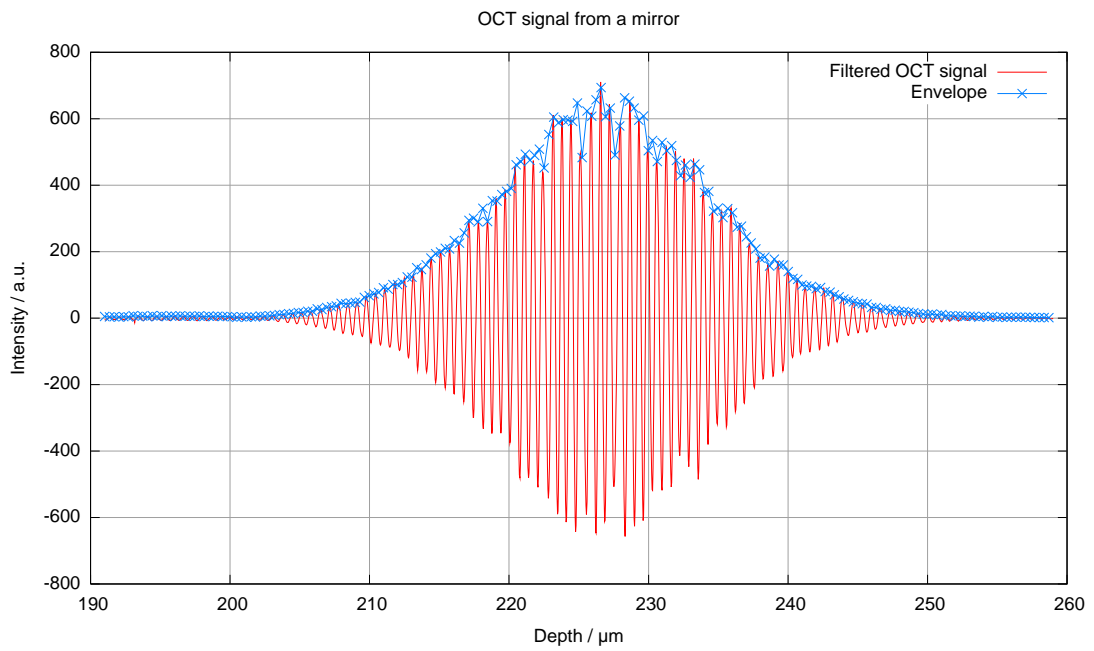
Figure 6.1. OCT signal from a mirror and its envelope (with crosses)
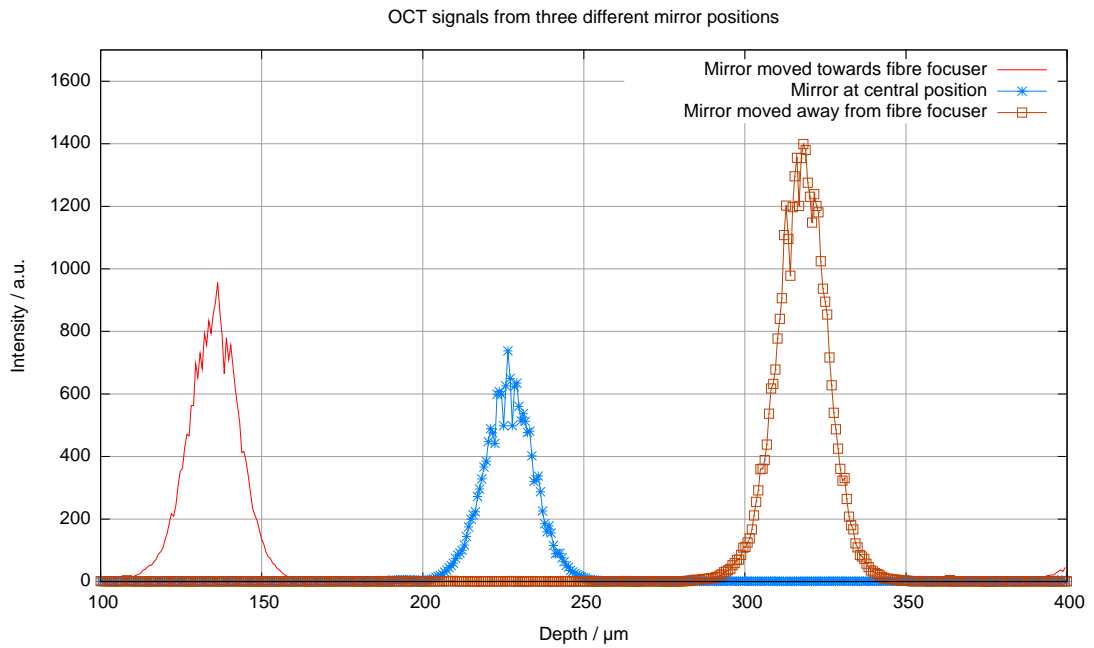

Figure 6.2. OCT signals from a mirror at three different positions

One more fact can be noticed in this figure: the signal strength varies with the distance between the focuser and the sample (see also section 6.4).

6.3. Repeatability

Fig. 6.3 shows the position of the signal's peak from 100 measurements performed on a mirror in the sample arm. The position varies unfortunately up to 13µm between two consecutive scans and shifts towards the positive z-direction.

Aligning the scans (see 5.2) reduced the fluctuation to at most $4\,\mu m$ between two consecutive scans and to less than $5\,\mu m$ in total (fig. 6.4).

6.4. Influence of the working distance

As already mentioned, the signal strength is influenced by the distance between the focuser and the sample (fig. 6.5). The strongest signal can be found at $1\,850\,\mu m$ which correlates with the lens's working distance of $1.7\,mm$.

6.5. Noise considerations

The signal intensity from a mirror located nearly at the working distance of the lens was $I_{\text{signal}} = 1\,272\,\text{a. u.}$ and the noise intensity $I_{\text{noise}} = 0.6731\,\text{a. u.}$. This gives a signal-to-noise ratio of

$$\text{SNR} = 10\log\left(\frac{I_{\text{signal}}}{I_{\text{noise}}}\right) = 10\log\left(\frac{1\,272\,\text{a. u.}}{0.6731\,\text{a. u.}}\right) = 32.8\,\text{dB} \qquad (6.1)$$

6.6. Microscope slide

Before presenting the results of the phantoms, the OCT signal from a SuperFrost microscope slide with a thickness of $d = 1.03\,mm$ shall be given (fig. 6.6).

The first peak stems from the lens, the second and third from the upside and the underside of the slide, respectively. The distance between those two is $\Delta z = 1\,541\,\mu m$ which leads to an index of refraction of $n = \frac{\Delta z}{d} = 1.50$.
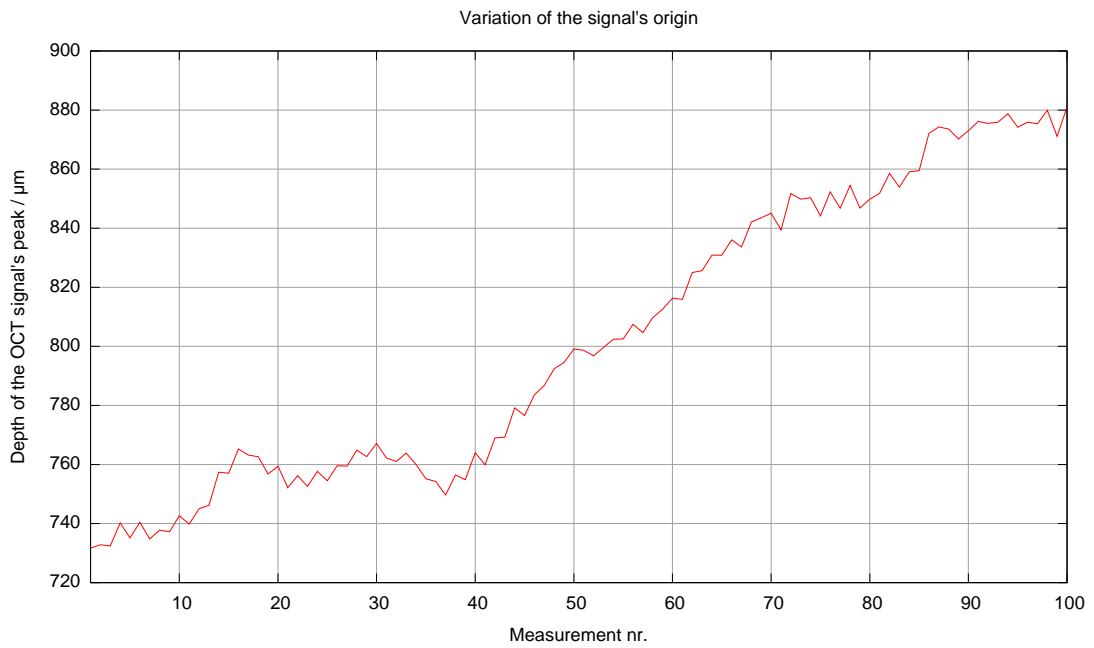
Figure 6.3. Variation of peak's position when multiple measurements are performed
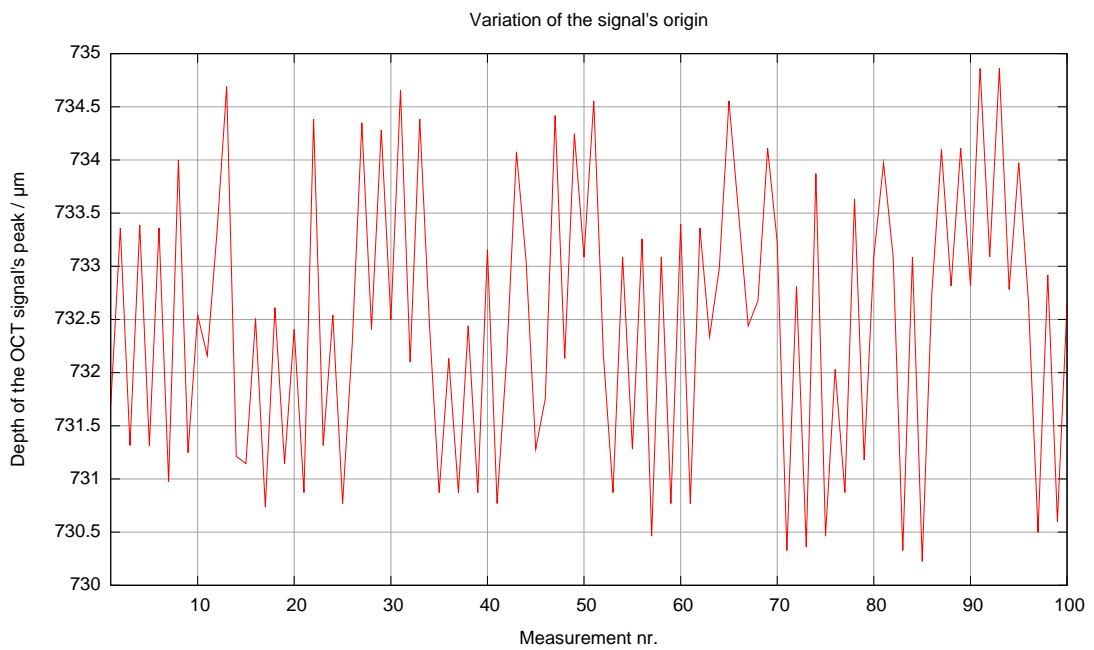

Figure 6.4. Variation of the OCT signal's position after aligning the scans to the sample lens
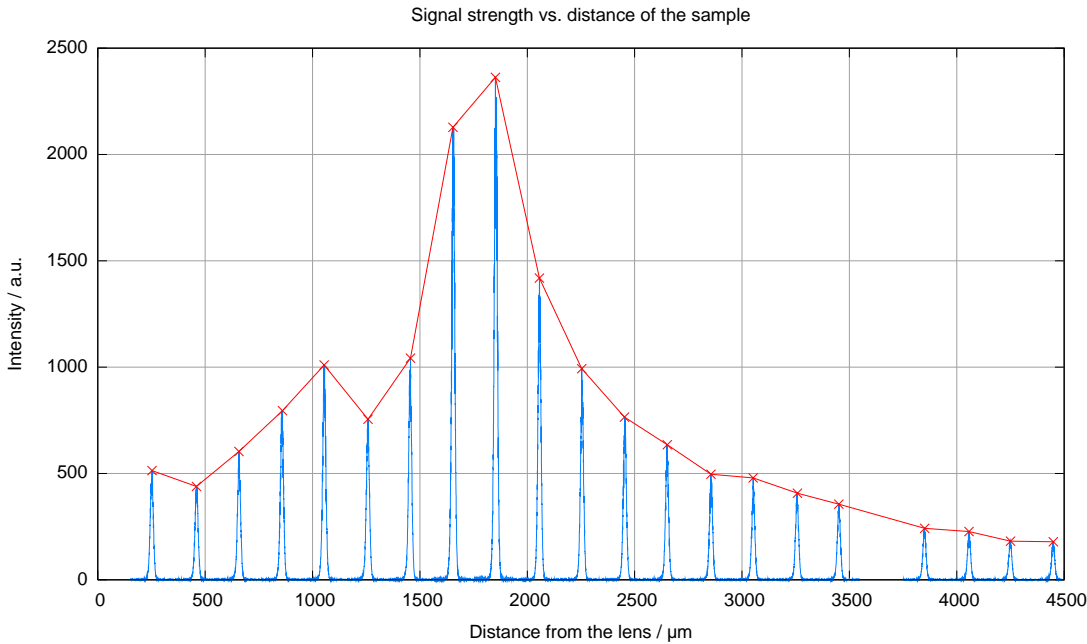
Figure 6.5. OCT signals from different working distances and the envelope of the maxima (with crosses)
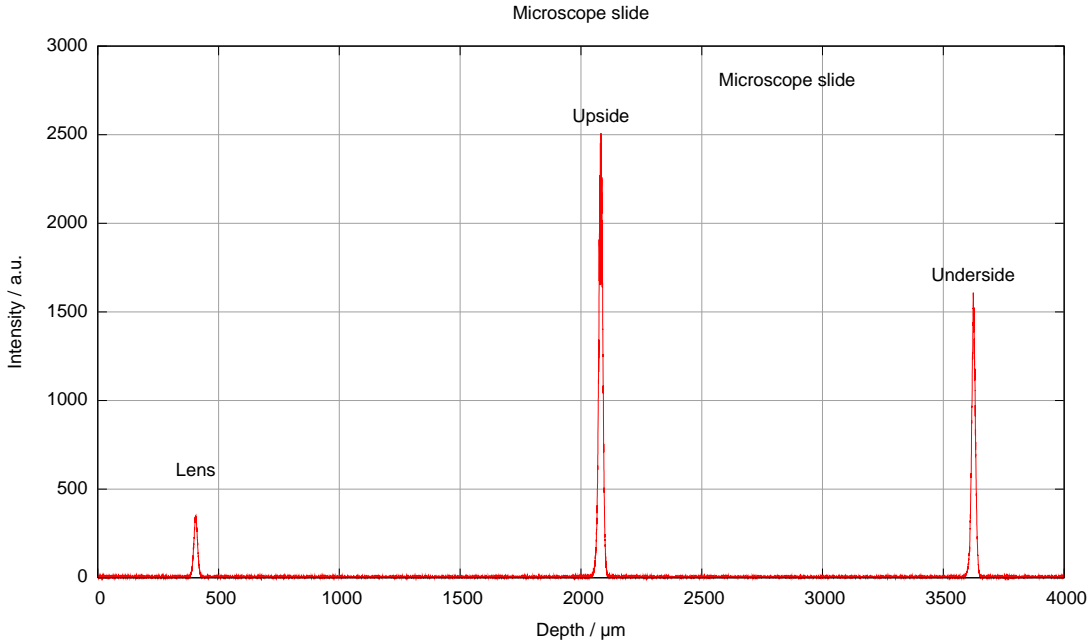

Figure 6.6. OCT signal from a microscope slide

6.7. Foil phantoms

The scans of the foil phantoms can be found on the pages 43–44. In fig. 6.7 and 6.8 one complete scan, including the reflection of the lens, can be seen. The other two figures show only the reflections from the foils. Otherwise they would be hard to distinguish.

If light bounces several times between the layers, it creates artefacts visible as additional peaks in the signal. Fig. 6.9 on page 44 is a good example for this effect. The three peaks after the last foil are such artefacts, for example.

Table 6.1 lists the minimum and maximum values of the measured thickness of each foil together with the corresponding refractive indices.

Foil	Min/max thickness µm	Min/max n
#27	106	1.68
	117	1.86
#47	61	1.69
	65	1.81
#67	104	1.65
	117	1.86
#89	60	1.66
	67	1.86

Table 6.1. Measured foil thicknesses and refractive indices

Table 6.2 on page 45 provides an overview about the position of the layer boundaries within the foil phantoms.
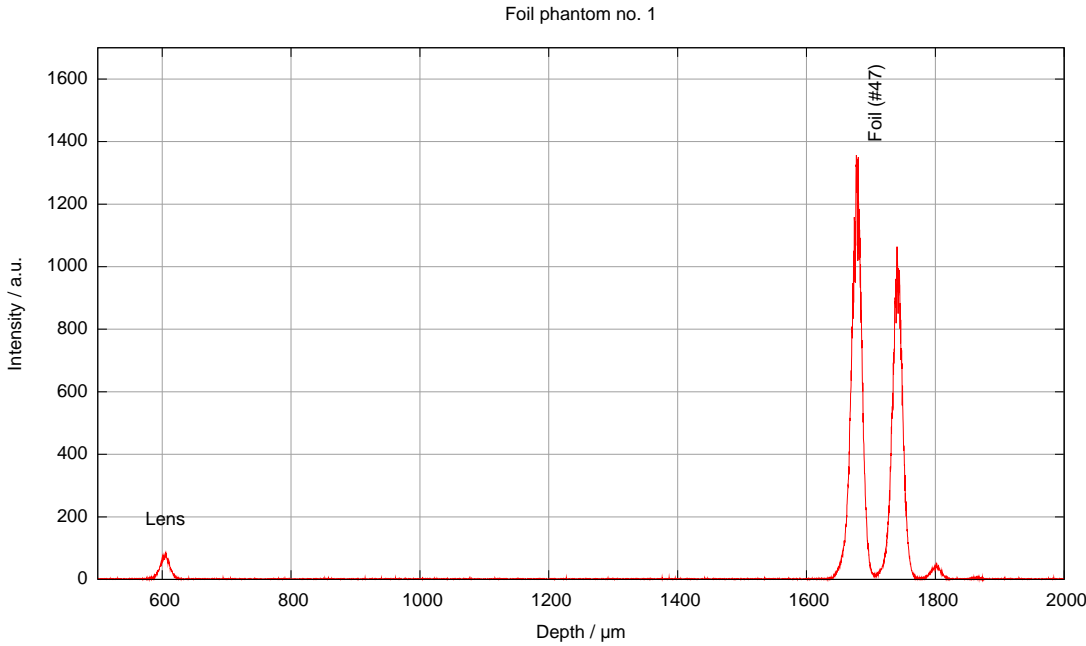
Figure 6.7. OCT signal from foil phantom no. 1
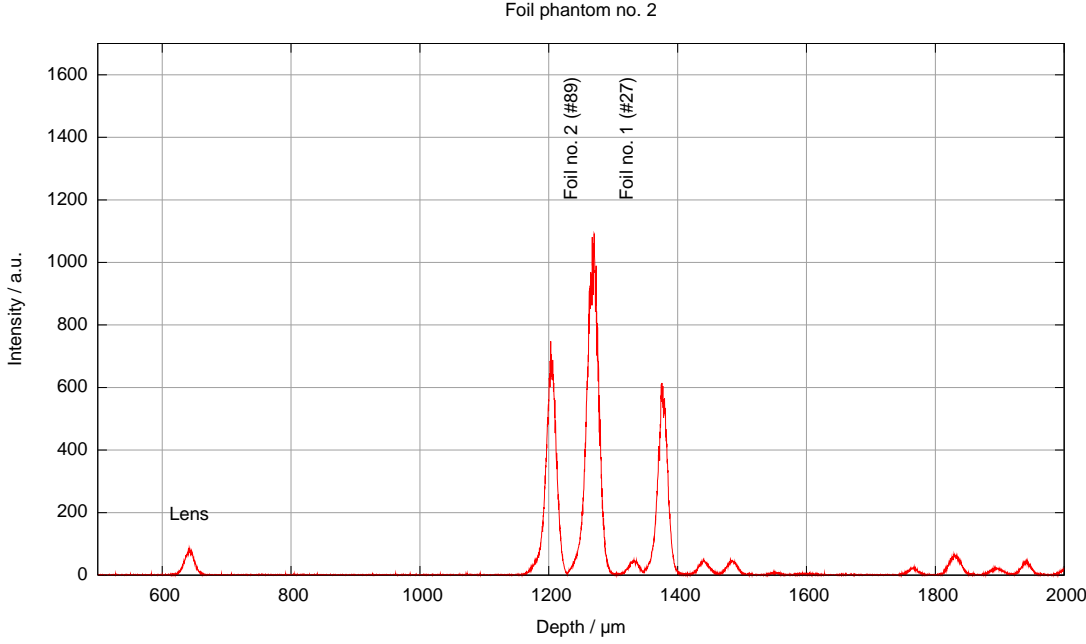
Figure 6.8. OCT signal from foil phantom no. 2
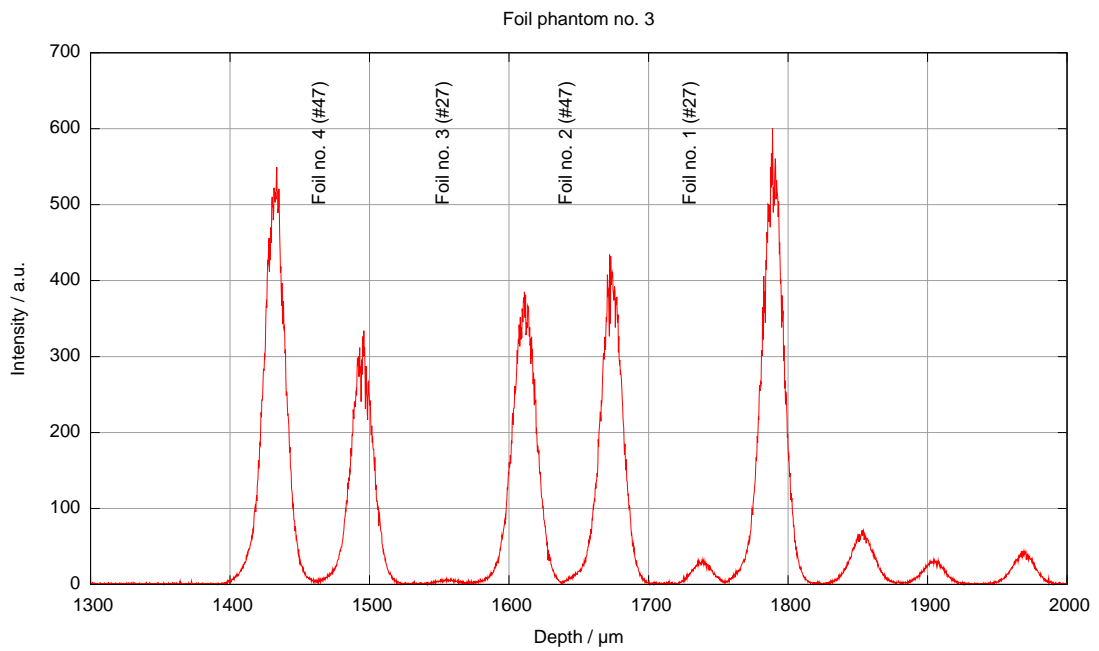
Figure 6.9. OCT signal from foil phantom no. 3
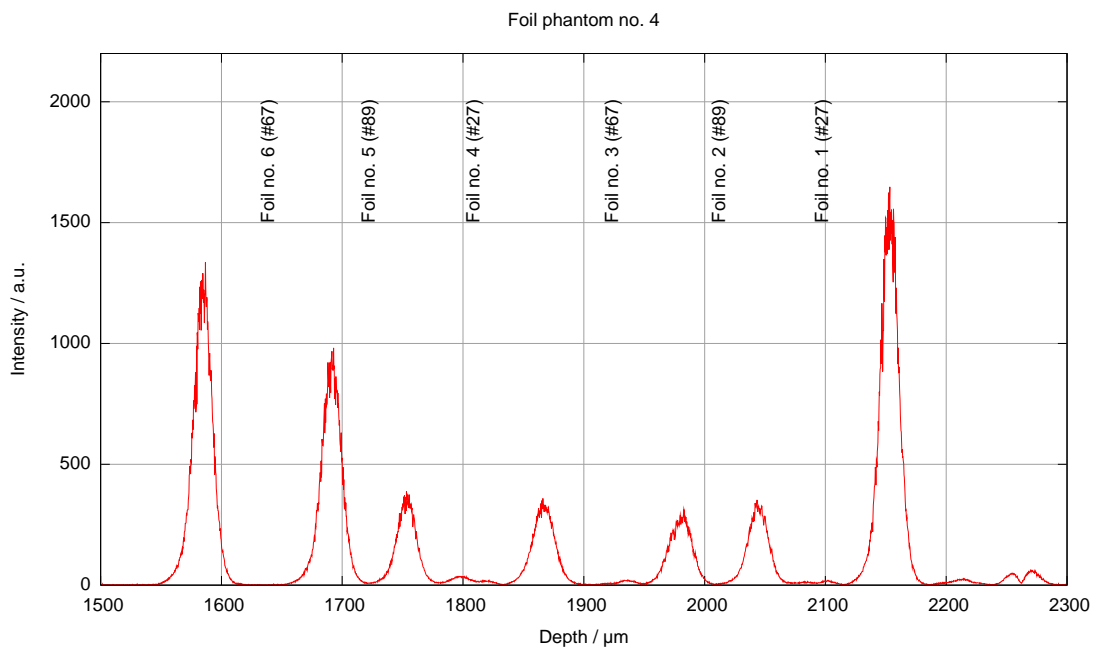
Figure 6.10. OCT signal from foil phantom no. 4

	Peak no.	Depth µm	Difference µm	Real foil thickness µm	n
Foil phantom 1	1 2	1 677 1 742	65	36	1.81
Foil phantom 2	1 2 3	1 203 1 270 1 376	67 106	36 63	1.86 1.68
Foil phantom 3	1 2 3 4 5	1 433 1 496 1 611 1 672 1 789	63 115 61 117	36 63 36 63	1.75 1.83 1.69 1.86
Foil phantom 4	1 2 3 4 5 6 7	1 587 1 691 1 753 1 866 1 983 2 043 2 153	104 62 113 117 60 110	63 36 63 63 36 63	1.65 1.72 1.79 1.86 1.66 1.75

Table 6.2. Measured position of the foil phantom's boundaries together with the refractive indices

6.8. Agar phantoms

The intensity of the backscatterings of the agar phantoms is much smaller compared to the foil phantoms. Nevertheless, the reflection from the microscope slide and the lens are of the same order of magnitude. Thus the denary logarithm of the intensity is plotted in fig. 6.11 and 6.12, to display the whole dynamic range.

It is not possible to locate the boundaries between the agar slices, and all six scans acquired look similar. Therefore, only two scans are reproduced in this section. Table 6.4 on page 48 lists the position of the reflections from the agar phantoms and the microscope slide for all six measurements and also the refractive indices obtained.

Table 6.3 shows the extreme values of the measured indices of refraction of the slide and agar phantoms. For the microscope slide, the minimum and maximum of the measured thickness is given, too. A detailed breakdown for the phantoms cannot be given since the different layers are not distinguishable.

	Min/max thickness µm	Min/max n
Agar phantom	inapplicable	1.36 2.03
Microscope slide	1 542 1 555	1.50 1.51

Table 6.3. Measured thicknesses of the agar phantoms and the microscope slide and the corresponding refractive indices
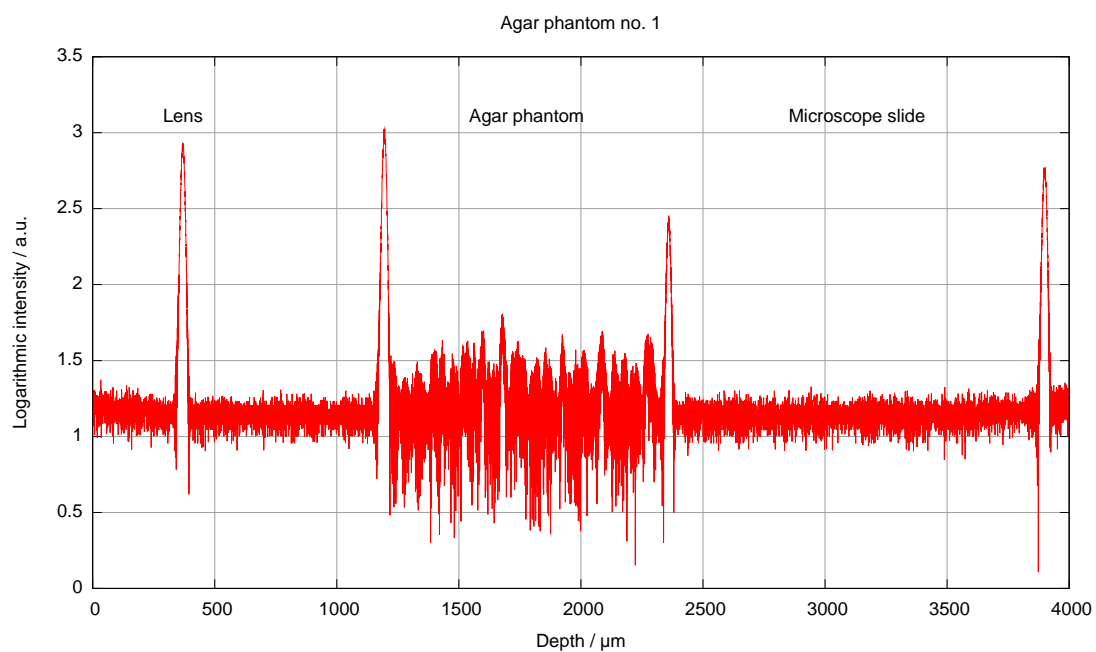
Figure 6.11. OCT signal from agar phantom no. 1
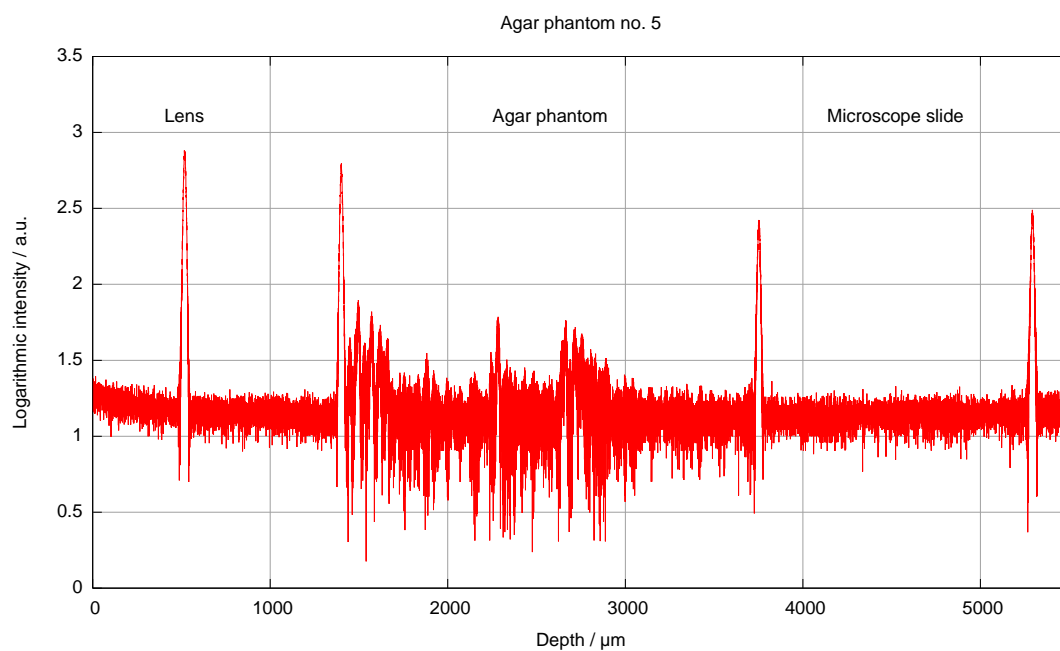
Figure 6.12. OCT signal from agar phantom no. 5

	Peak no.	Depth	Difference	Real phantom/ slide thickness	n
		µm	µm	µm	
Agar phantom 1	1 2 3	1 196 2 360 3 902	1 164 1 542	800 1 030	1.46 1.50
Agar phantom 2	1 2 3	824 3 549 5 096	2 725 1 548	2 000 1 030	1.36 1.50
Agar phantom 3	1 2 3	1 172 3 604 5 159	2 432 1 555	2 000 1 030	2.03 1.51
Agar phantom 4	1 2 3	747 3 888 5 435	3 141 1 547	2 000 1 030	1.43 1.51
Agar phantom 5	1 2 3	1 401 3 751 5 293	2 350 1 542	1 400 1 030	1.68 1.50
Agar phantom 6	1 2 3	1 949 3 851 5 393	1 902 1 542	1 400 1 030	1.36 1.50

Table 6.4. Measured position of the boundaries of the agar phantoms and the microscope slide together with the indices of refraction

Chapter 7.

Discussion and conclusions

An A-scan OCT system in time domain has been implemented and evaluated. Objects with a thickness as low as 36 μm can be identified without problems (fig. 6.7). This is not the limit of the system, yet, but is the thinnest quite well defined object available. Further investigations have to be done to see if structures with sizes near the round trip coherence length can still be resolved.

The shape of the envelope is Gaussian as it is predicted by theory. The fact that it is not a perfect Gauss curve has mainly two reasons. First, noise from various sources—shot noise, amplifier noise, influences from the power system and so on—disturbs the signal's quality. Second, it was assumed that the spectrum of the light source is perfectly Gaussian, too. If this assumption is not valid, the OCT signal's envelope will also change its shape[7].

Method

The advantage of the time domain implementation is that it does not need an expensive spectrometer and detection array contrary to a Fourier domain implementation. Furthermore, the frequency of the measured signal is adjustable through the motor speed and can thus be set to allow for a simple design of the detection electronics.

The scan range can be chosen simply by varying the start and stop position of the delay line's reference mirror. Also the signal processing can be reduced to a minimum.

Less advantageous with time domain is the long scan time required since the reference mirror has to move a distance equivalent to the scan range. In contrast, a Fourier domain OCT acquires one complete line at once without the need of moving parts at the cost of advanced signal processing[7].

Considering the beam splitter, the chosen interferometer configuration is not ideal as half of the backscattered light is led back to the source instead of being detected. This reduces the sensitivity of the system in an unnecessary manner.

A better choice would be a beam splitter with an uneven splitting ratio, which allowed to send more light into the sample than the reference arm. Another remedy would be the use of an optical circulator as shown in fig. 3.1.

Analogue signal processing

The analogue signal processing is built modularly to make it easily modifiable and extensible. The tunable non-inverting amplification boosts the detected OCT signal to use the full dynamic range of the A/D transducer.

The selected order of the filtering and amplification stages is sub-optimal at the moment since the last amplifier boosts not only the signal wanted but also the noise of the previous modules. A solution would be to use balanced detection where the background intensity is filtered out early in the signal processing chain. The amplification could then be done before the filtering which should result into a better SNR.

As can be seen in fig. 6.11 and 6.12, the intensity differs several orders of magnitude, depending on whether the signal stems from reflection or backscattering. However, the transimpedance amplifier has just a linear characteristic. In the system it was desired to map the whole range of the photo diode to the A/D converter range. Of necessity, this leads to a limited sensitivity.

A logarithmic amplifier would suit better in this particular case as weaker signals are weighted more compared to stronger. A proposal for an adapter for a logarithmic amplifier can be found in appendix G.

Sample focuser

The sample focuser from OECA does not work on scattering sample media, probably due to an unmatched numerical aperture at the fibre side that prevents backscattered light from being launched into the fibre again.

The selection of the GRIN rod lens yields satisfactory results for reflective surfaces like filter foils. The high NA collects a large part of the reflections and backscatterings, and thus facilitates the detection of discontinuities. It also has the benefit that the sample beam has a small beam waist in the focal plane[7] which is a prerequisite for a good lateral resolution.

However, it can be shown that the probing depth and the image contrast decrease with a higher numerical aperture since the probability of collecting multiple scattered photons rises[7, 24]. Desirable is an implementation with a low numerical aperture at the focuser's sample side and a numerical aperture equal to the one of the single mode fibre at the fibre side.

This could be achieved when the FC/PC focuser was replaced by a combination of a FC/PC collimator and an additional focusing lens.

Digital signal processing

The digital signal processing is implemented only in a very rudimentary manner. The Hilbert transform has been selected since it does not require additional low-pass filtering as it is the case if the envelope is calculated by rectification[6].

To enhance the OCT image quality, various filtering techniques can be used. The simplest method is to deconvolve the measured signal with the impulse response of an ideal reflector[7]. Even better outcomes can be obtained using iterative methods like the CLEAN algorithm, for example, a highly non-linear point-deconvolving technique[17].

Also more effort can be applied on the detection of the lens's pattern in the scans. In the current version, the user still has to specify the starting search range and the algorithm will fail if the variations between two scans are too high.

Phantoms

The fabrication of the phantoms was a tedious and time-consuming process. Unfortunately, the agar phantoms produced, have not reached the quality expected beforehand. The ink has not dissolved completely, leaving small black particles in the agar substrate. Of course, this will have impact on the optical properties and destroy the homogeneity of the phantoms.

Probably also the agar slice thickness after cutting with the Vibratome® is not exact. This argument is supported by the fact that the refractive index of the agar phantoms varies from 1.36 to 2.03, whereas the one of the microscope slide is rather constant around 1.50. According to Hartleb[25], the index of refraction should match the one for water. This is only the case for phantoms no. 2 and 6 (table 6.4).

The boundaries between the agar layers cannot be located. One explanation is the noise and the limited system sensitivity. The other is that the optical parameters μ'_s and μ_a, respectively, do not differ as much as intended since they

were calculated for a wavelength of $633\,\text{nm}$. For a wavelength of $1300\,\text{nm}$ the properties of the agar phantoms are not known at the present time.

The slices have been stacked immediately after being cut under water with the Vibratome®. Probably the water between the slices matches the refractive indices of the different agar materials, which lowers the amount of backscattered light at that site.

The only conclusion that can be drawn from the agar phantom scans (fig. 6.11 and 6.12) is that the agar medium is scattering as there are peaks (noise) throughout the whole layer and not just at the upside and underside, respectively, as in the case of microscope slides (fig. 6.6).

However, the results from the foil phantoms are quite promising. The extrema of the measured thicknesses differ by approximately $10\,\%$. One reason for this is that the maximum of a peak defines the depth. This maximum can be located at different positions within the signal because of added noise. Therefore, another measure, e.g. the mean value of the half-maximum positions or a correlation measure, could yield better results. Of course, a second explanation could be that the foils themselves are not precise enough in thickness as this is not their primary property.

Conclusion

Summarising, it can be said that the system performs well on reflective surfaces. It has been shown that structures with a size down to $36\,\mu\text{m}$ and less are resolvable. Deeper analysis was unfortunately prevented due to the lack of high-quality phantoms.

Chapter 8.

Prospect

The system is still in its early stages, so there are various possibilities to enhance it.

As seen in the results chapter, one limitation is set by the sensitivity of the transimpedance amplifier. The amplifier could be changed rather easily as proposed in appendix G.

The motor is controlled in a quite primitive manner now, making exact positioning difficult or even impossible. The algorithm should consist of a closed loop controller which takes the motor's position, speed and acceleration into account. Furthermore, the motion sequence should probably be trapezoidal, which means a constant acceleration and slowing down and a linear motion in between.

The system already has a built-in H-bridge for a second motor that can be used to move the sample transversally. Thus the imaging modality can be extended to a second dimension. Fig. 8.1 shows an early B-scan image of a foil phantom.
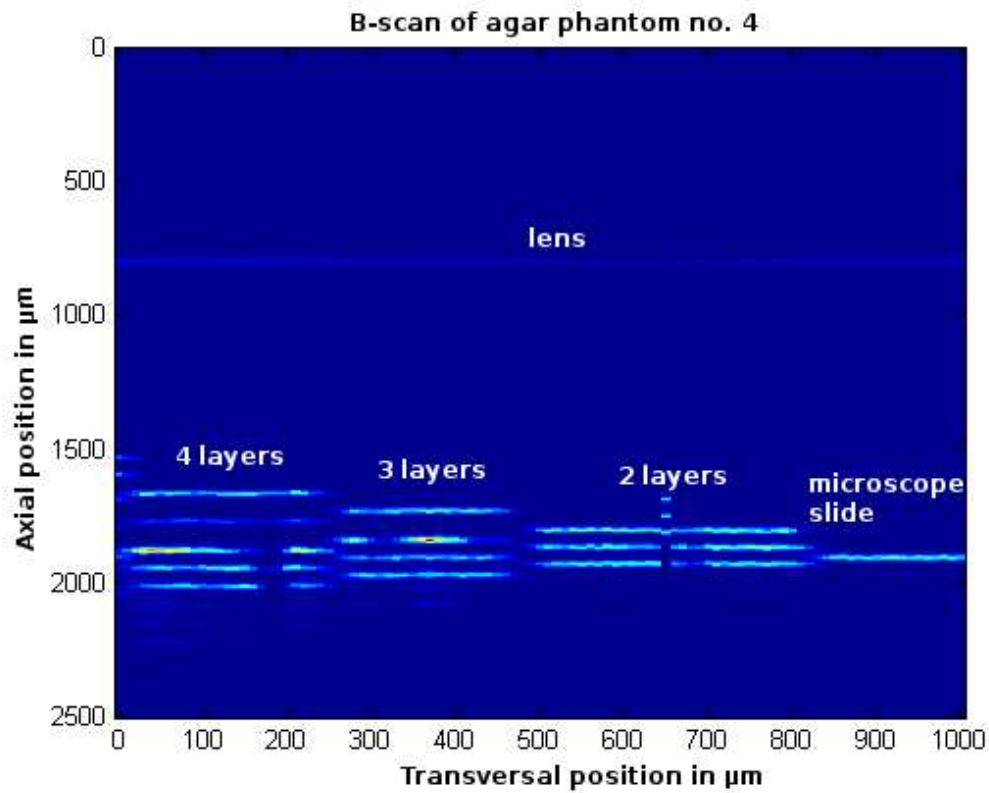
Figure 8.1. B-scan of foil phantom no. 4: The foils were stacked to form a stair. The foil layers seem to be shifted in depth since the scans were aligned along the lens, and the measured distances vary owing to the different refractive index of the foil and air.

Bibliography

[1] Huang D, Swanson EA, Lin CP, Schuman JS, Stinson WG, Chang W, et al. Optical Coherence Tomography. Science 1991;254(5035):1178–1181.

[2] Conolly S, Macovski A, Pauly J, Schenck J, Kwong KK, Chesler DA, et al. Magnetic Resonance Imaging. In: Bronzino JD, editor. The Biomedical Engineering Handbook. 2nd ed. Boca Raton, USA: CRC Press LLC; 2000. p. 63/1–63/16.

[3] Goldberg RL, Smith SW, Mottley JG, Ferrara KW. Ultrasound. In: Bronzino JD, editor. The Biomedical Engineering Handbook. 2nd ed. Boca Raton, USA: CRC Press LLC; 2000. p. 65/1–65/41.

[4] Brezinski ME, Fujimoto JG. Optical Coherence Tomography: High-Resolution Imaging in Nontransparent Tissue. IEEE Journal of Selected Topics in Quantum Electronics 1999;5(4):1185–1192.

[5] Fujimoto JG. Optical Coherence Tomography: Introduction. In: Bouma BE, Tearney GJ, editors. Handbook of Optical Coherence Tomography. New York, USA: Marcel Dekker, Inc; 2001. p. 1–40.

[6] Hee MR. Optical Coherence Tomography: Theory. In: Bouma BE, Tearney GJ, editors. Handbook of Optical Coherence Tomography. New York, USA: Marcel Dekker, Inc; 2001. p. 41–66.

[7] Fercher FA, Drexler W, Hitzenberger CK, Lasser T. Optical coherence tomography—principles and applications. Reports on Progress in Physics 2003;66:239–303.

[8] Bruno O, Chaubell J. One-dimensional inverse scattering problem for optical coherence tomography. Inverse Problems 2005;21:499–524.

[9] Hecht E. Optics. 4th ed. San Francisco, USA: Addison Wesley; 2002.

[10] Fuji T, Miyata M, Kawato S, Hattori T, Nakatsuka H. Linear propagation of light investigated with a white-light Michelson interferometer. Journal of the Optical Society of America B 1997;14(5):1074–1078.

[11] Mobley J, Vo-Dinh T. Optical Properties of Tissue. In: Vo-Dinh T, editor. Biomedical Photonics Handbook. Boca Raton, USA: CRC Press LLC; 2003. p. 2/1–2/75.

[12] Oregon Medical Laser Center [homepage on the Internet]. Definition and units of absorption coefficient; 1998 [cited July 31, 2005]. Available from: http://omlc.ogi.edu/classroom/ece532/class3/muadefinition.html.

[13] Oregon Medical Laser Center [homepage on the Internet]. Scattering; 1998 [cited July 31, 2005]. Available from: http://omlc.ogi.edu/classroom/ece532/class3/scattering.html.

[14] Oregon Medical Laser Center [homepage on the Internet]. Scattering functions; 1998 [cited July 31, 2005]. Available from: http://omlc.ogi.edu/classroom/ece532/class3/ptheta.html.

[15] Oregon Medical Laser Center [homepage on the Internet]. Definition of anisotropy; 1998 [cited July 31, 2005]. Available from: http://omlc.ogi.edu/classroom/ece532/class3/gdefinition.html.

[16] van Gemert MJC, Jacques SL, Sterenborg HJCM, Star WM. Skin Optics. IEEE Transactions on Biomedical Engineering 1989;36(12):1146–1154.

[17] Izatt JA, Rollins AM, Ung-Arunyawee R, Yazdanfar S. System Integration and Signal/Image Processing. In: Bouma BE, Tearney GJ, editors. Handbook of Optical Coherence Tomography. New York, USA: Marcel Dekker, Inc; 2001. p. 143–174.

[18] iSixSigma [homepage on the Internet]. Term Definition: Repeatability; [updated July 18, 2002; cited June 28, 2005]. Available from: http://www.isixsigma.com/dictionary/Repeatability-311.htm.

[19] Stewart G. Principles of Modern Optical Systems—Basic Optics and Opto-electronics. In: Andonovic I, Uttamchandani D, editors. Principles of modern optical systems. Norwood, USA: Artech House, Inc; 1989. p. 7–33.

[20] Fiber Connections [homepage on the Internet]. Glossary; [cited May 1, 2005]. Available from: http://www.fiberc.com/glossary.asp.

[21] developers.net [homepage on the Internet]. Measure code sections using the Enhanced Timer; 2004 [cited July 30, 2005]. Available from: `http://www.developers.net/external/548`.

[22] Johnstone W. Optical Detection. In: Andonovic I, Uttamchandani D, editors. Principles of modern optical systems. Norwood, USA: Artech House, Inc; 1989. p. 99–128.

[23] Deliyannis TL, Sun Y, Fidler JK. Continuous-Time Active Filter Design. Boca Raton, USA: CRC Press LLC; 1999.

[24] Karamata B, Leutenegger M, Laubscher M, Bourquin S, Lasser T. Multiple scattering in optical coherence tomography. II. Experimental and theoretical investigation of cross talk in wide-field optical coherence tomography. Journal of the Optical Society of America A 2005;22(7):1380–1388.

[25] Hartleb C. Creation and Evaluation of Solid Optical Tissue Phantoms for Bio-medical Optics Applications [project report]; 2005. LiTH-IMT/ERASMUS-R--05/28--SE. Available from: `http://www.ep.liu.se/`.

[26] Martini FH. Fundamentals of Anatomy & Physiology. 6th ed. San Francisco, USA: Pearson Education, Inc; 2004.

[27] Granlund GH, Knutsson H. Signal Processing for Computer Vision. Dordrecht, NL: Kluwer Academic Publishers; 1995.

Appendix A.

SLD communication protocol

The communication with the SLD was made through a RS232 port. The commands were sent to the evaluation board in plain ASCII format with eight bit data. Table A.1 gives a summary of the port settings.

Transfer rate	9 600 bd
Data bits	8
Stop bits	1
Parity	none
Data format	ASCII
Connection scheme	DTE

Table A.1. RS232 settings for the SLD

Every command was terminated by a carriage return (*CR*, ASCII: 0Dh). The board sent back an echo of the command including the *CR* plus a trailing line feed (*LF*, ASCII: 0Ah). Afterwards the response followed which could be OK as an acknowledgement or the value of the desired parameter. That answer was terminated by *LF* *CR*. Note that the sequence of *CR* and *LF* was reversed compared to the echo termination. Next follows a detailed description of the commands.

Switching on and off

To switch the diode on, just a y with the termination character had to be sent to the evaluation board. The board answered with an echo and the sequence OK.

TX: y *CR*
RX: y *CR* *LF* OK *LF* *CR*

The switch-off worked analogous and was coded by a `n`.

```
TX: n CR
RX: n CR LF OK LF CR
```

Setting the TEC set-point

When setting the desired operating temperature T, it had to be coded as a 16-bit integer value. The code words for all possible temperature values between $10\,°C$ and $40\,°C$ were read from the serial port. Afterwards equation (A.1) was found to be a good approximation for the values to be sent. The error between the real and the estimated value was within -1 and $+2$.

The coded temperature had to be split into higher and lower byte and transfered via the serial port using the command `p`. The board acknowledged this command then.

$$coded = \mathrm{round}\left(\frac{82\,°C - T}{82\,°C - (\text{-}30\,°C)} \cdot 1\,024\right) \tag{A.1}$$

$$HI = \left\lfloor \frac{coded}{256} \right\rfloor$$

$$LO = coded \bmod 256$$

Next the command `w ␣ 52` had to follow, which was again acknowledged by the evaluation board. The meaning of this command could not be found out.

```
TX: p ␣ HI ␣ LO CR
RX: p ␣ HI ␣ LO CR LF OK LF CR
TX: w ␣ 52 CR
RX: w ␣ 52 CR OK LF CR
```

Reading the temperature

To read the temperature sensor on the evaluation board, the parameter no. 166 had to be read using the command `g`.

```
TX: g ␣ 166 CR
RX: g ␣ 166 CR LF HI ␣ LO LF CR
```

HI and *LO* were two 3-digit numbers with leading zeros if needed and were the high and the low byte of the coded temperature, respectively. The temperature T in ℃ could be calculated by

$$coded = \mathit{HI} \cdot 256 + \mathit{LO}$$

$$T = 82\,°\text{C} - \frac{coded}{1\,024} \cdot (82\,°\text{C} - (\text{-30})\,°\text{C}) \tag{A.2}$$

Setting the current

The command s was used to set the supply current I for the superluminescent diode. Again the value was not transfered in a plain format but coded by dividing by $0.4\,\text{mA}$ and splitting in the high and the low byte.

$$coded = \text{round}\left(\frac{I}{0.4\,\text{mA}}\right) \tag{A.3}$$

$$HI = \left\lfloor \frac{coded}{256} \right\rfloor$$

$$LO = coded \bmod 256$$

TX: s ␣*HI*␣*LO CR*
RX: s ␣*HI*␣*LO CR LF* OK *LF CR*

Reading the current

Analogous to the reading of the temperature, the parameter no. 164 had to be read to determine the current of the SLD.

TX: g ␣164 *CR*
RX: g ␣164 *CR LF HI*␣*LO LF CR*

Again *HI* and *LO* were two 3-digit numbers with leading zeros if needed. The current I was decoded using the next equation.

$$coded = 256 \cdot HI + LO \tag{A.4}$$

$$I = 0.4\,\text{mA} \cdot coded$$

Setting constant current mode

Setting the board to constant current mode could be accomplished by sending the c command. The board acknowledged this with an OK.

```
TX: c CR
RX: c CR LF OK LF CR
```

Reading a setting

The full meaning of the command r could not be found out, as it was only used two times during the initialisation sequence. However, it seemed that it was used to read some factory-set parameter, because the return values remained the same all the time. Important was also that there was an additional *CR* between the echo sequence and the response. The two usages were in detail:

```
TX: r ⊔ 8 CR
RX: r ⊔ 8 CR LF CR 008 LF CR
```

```
TX: r ⊔ 102 CR
RX: r ⊔ 102 CR LF CR 001 LF CR
```

Reading board specific data

With the command d board specific data could be retrieved. Two different versions were available. If no number followed, the board would send its own identification string.

```
TX: d CR
RX: d CR LF Kamelian OPA Controller 1.13 LF CR
```

If an integer number followed, a string from a data block was read. The valid range for *no* seemed to be 0–32. The length of the answer string *string* was always 19 characters.

```
TX: d ⊔ no CR
RX: d ⊔ no CR LF string LF CR
```

Appendix B.

Alignment of the delay line

Aligning the fibre bench, fibre port and mirror port was a tricky and time consuming process since the infrared light was not visible. Thus a phosphorus detector card was used. The following list of tasks should provide some help to align the parts again if needed.

1. On the fibre port, loosen the three recessed black socket-head cap screws. Next tighten them very softly until a small resistance is sensible. Now the ray should be parallel to the fibre bench.

2. Do the same with the black screws of the mirror port. The mirror should be perpendicular to the ray now.

3. Make the ray visible with a detector card and turn the fibre port's X-Y adjustment screws until the beam hits the mirror.

4. If the mirror is aligned well enough, the ray will already be reflected back to the fibre port. Otherwise it could be helpful to tighten one screw as much as possible, and to search for the reflection with the help of the detector card. Then the three screws have to be adjusted until the light is led back to the fibre port.

5. Tighten the three black screws of the fibre port equally in $\frac{1}{4}$-turn increments until the detector shows an answer.

6. To make the ray parallel, which means that the fibre end has to be in the focal plane of the fibre port's collimating lens, adjust X-Y and the black screws alternatively. The beam will be parallel if the detector answer is the same regardless of the sledge's position on the bench. If the beam is divergent, the answer will be bigger the nearer sledge is to the collimator. If it is convergent, the answer is bigger the greater the distance between the mirror and the fibre port is.

7. To avoid unwanted changings in the alignment, fix the fibre port with the help of the fixation screw. This has to happen very carefully and the X-Y screws have to be adjusted iteratively, too, as otherwise the alignment is lost.

Appendix C.

Instruction manual

The following list describes the function of all elements of the program written in LabVIEW™. The screen shot can be found on page .

1. **DAQCard no:** Set the number of the DAQCard-700. The number can be chosen in National Instrument's Measurement and Automation Explorer.

2. **SLD serial port:** Set the RS232 port that is attached to Kamelian's SLD evaluation board.

3. **Connect:** Press this button to establish the connection to the DAQCard-700 and the SLD evaluation board.

4. **Stop:** Press this button to stop the program.

5. **SLD current:** Set the current that shall drive the SLD. Possible values range from 0 to 250 mA.

6. **SLD temperature:** Set the temperature the SLD shall be operated at. The values range from 10 ℃ to 40 ℃.

7. **Hysteresis:** Set the hysteresis the TEC shall be operated with. The TEC will be switched on, if the SLD's temperature lies above 'SLD temperature' + 'hysteresis' and switched off if it is below 'SLD temperature' − 'hysteresis', respectively.

8. **SLD power:** Switches the SLD on and off, respectively. The current status is indicated by the green light.

9. **Current read:** The momentary value of the SLD current as it is sent by Kamelian's SLD evaluation board.

10. **Temperature read:** The feedback value of the temperature of the SLD.

11. **TEC status:** A green light indicates that the TEC is powered on at the moment.

12. **Motor steps/mm:** This value tells the program, how many steps the motor has to move per millimetre.

13. **Steps to move:** This value tells the program, how many steps to advance if either one of the next two buttons is pressed.

14. **<:** If this button is pressed, the motor will move the amount of steps set in the field 'steps to move' backward.

15. **>:** Analogous, this button will move the motor by 'steps to move' steps forward.

16. **Set origin:** If this button is pressed, the current motor position will be set to zero. Thus a new origin for the measurements is defined.

17. **Motor position (steps):** This is the current motor position in steps.

18. **Motor position (mm):** This is the momentary motor position in millimetres.

19. **Scan start:** This tells the program, at which step it shall start the scan.

20. **Scan end:** This value is where the program stops the scan.

21. **Scan extend:** This is the number of steps, the program will record before the actual start and end. So the scan will start at 'scan start' − 'scan extend' and stop at 'scan end' + 'scan extend'. The additional samples before 'scan start' and after 'scan end' will be cut away by the MATLAB® program. This parameter is particularly useful to compensate for the motor power-up phase.

22. **Sample interval:** Set here the sampling interval of the DAQCard-700 in µs. This value is the time between two samples from two different channels. The channels themselves are sampled in a round-robin sequence. As actually three channels have to be sampled, each one has a sample interval that is three times the value entered in this field.

23. **Amount of scans:** This tells the program, how many A-scans to perform.

24. **A-scan:** Starts the A-scans. Check once more all values before pressing this button as it can take some time until all scans are finished.

25. **Yellow light:** This light is on if the scan has not been saved, yet.

26. **Save:** Press this button to write the last scan into a text file.

27. **Motor speed:** Set here the motor speed in mm/s. This value affects only the appearance of the graph below as it converts from sampling time to distance. The parameter has no effect on any MATLAB® script as they use the information from the motor's encoder signals to determine the distance.

28. **Graph:** Here the last scan can be seen. The conversion between sampling time and distance is done with the parameter 'motor speed'.

29. **Graph tools:** Use these tools to zoom into the graph, move its origin etc.

30. **Real start:** In this array the real start steps can be seen. They will be used in the MATLAB® scripts to determine the offset of the first motor step.

31. **Real end:** This array contains the end points of all scans and is used in MATLAB®, too.

32. **Array length:** This array holds the lengths of all scans and is also used in MATLAB®.

33. **Scan:** This three-dimensional array contains the last scan. The first dimension is the scan number, the second the sampling channel and the third the sampling time.

34. **Detector value:** Here the current value from the detector is shown before it is filtered with the analogue band-pass filter. This value can be used to determine if an interference signal is present without the need of a moving motor.
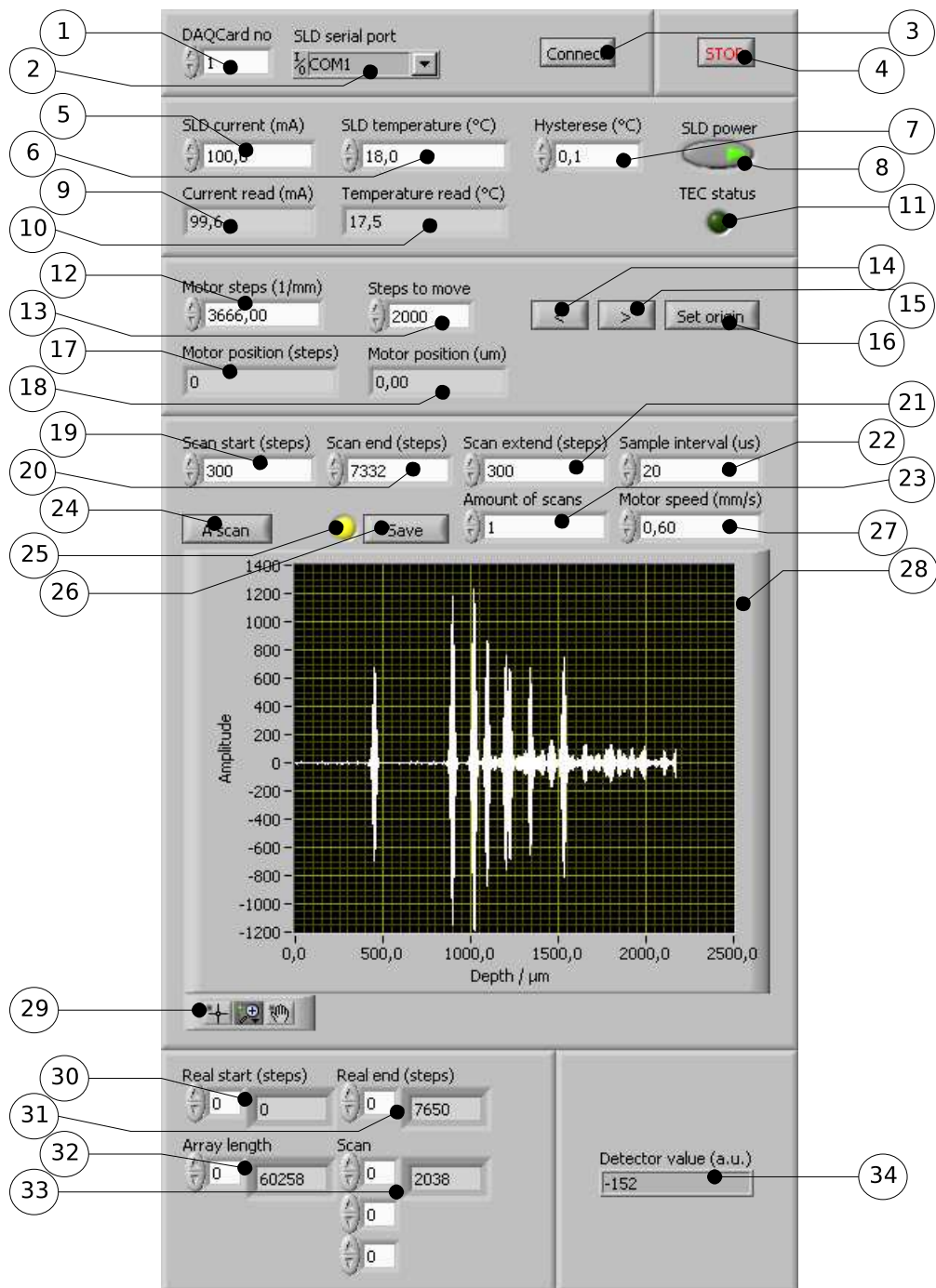
Figure C.1. Screen shot of the LabVIEW™ program

Appendix D.

MATLAB® scripts

The next table lists the script written for the project. Fig. D.1 shows a flow chart of the scripts

Script	Task
AScan	converts motor steps to µm and calculates the envelope
downsampleAScan	extracts the samples at full motor steps
filterAScan	applies a median filter on the envelope
findLens	locates the lens in the A-scan
plotAScan	plots the scan
readAScanFile	imports the LabVIEW™ output file into MATLAB®
repositionAScan	shifts the depth of the scan
reverseAScan	sorts the scan if necessary so that the depth is ascending

Table D.1. Overview about the MATLAB® scripts
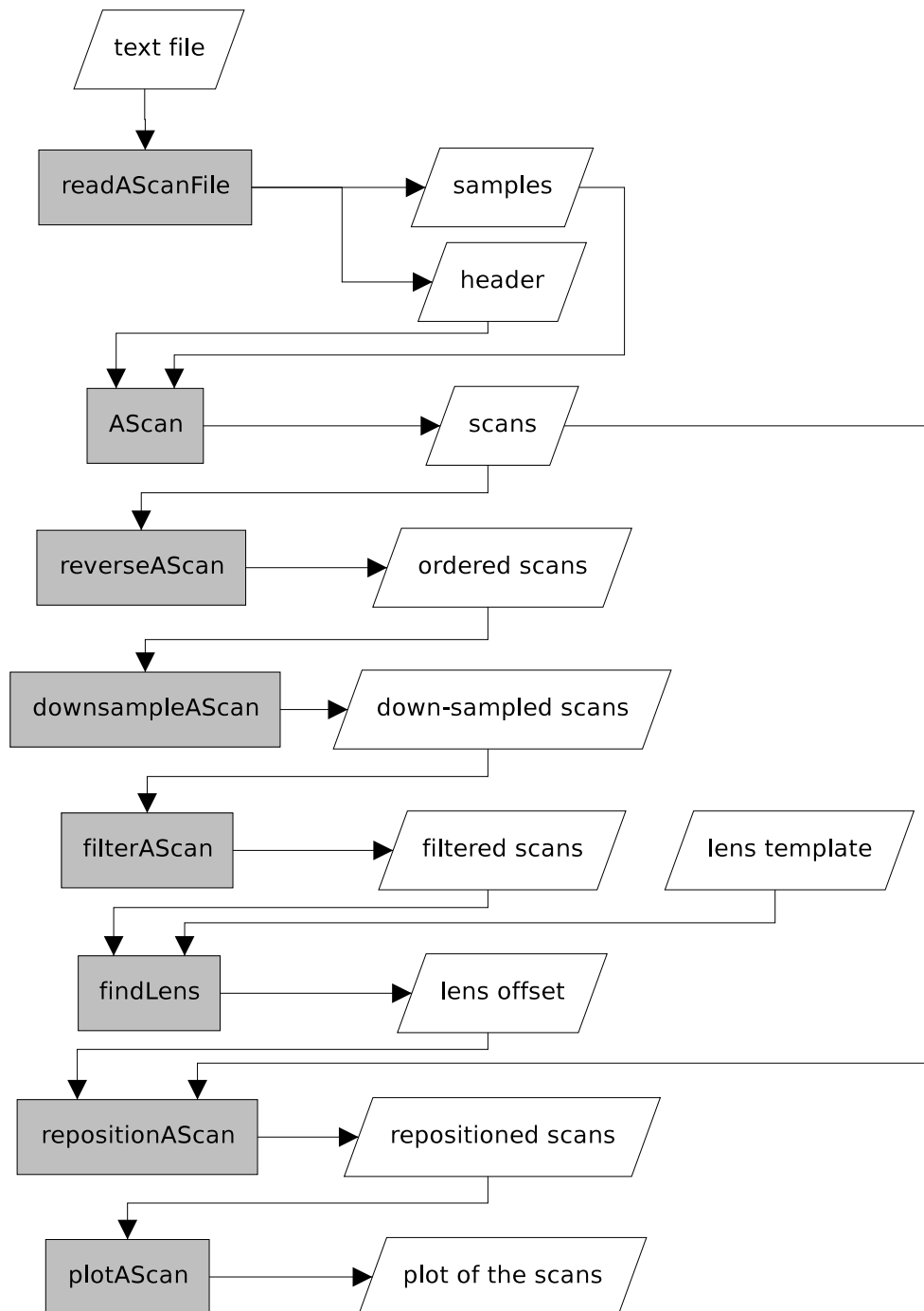
Figure D.1. Flow chart of the MATLAB® scripts

Appendix E.

DAQCard pin assignment

In this section, the pin assignment of the DAQCard-700 is listed to facilitate the enhancement of the system and/or changes in the software. Pins not listed in the following table were not used in the system and are thus available for other purposes.

Pin no.	Pin name	Function
1	AIGND	Analogue ground
2	AIGND	Analogue ground
3	ACH0	Filtered detector signal
5	ACH1	Axial motor, encoder A channel
7	ACH2	Axial motor, encoder B channel
9	ACH3	Unfiltered detector signal
19	DGND	Digital ground
30	DOUT0	Axial motor, PWM pin
31	DOUT1	Axial motor, DIR pin
32	DOUT2	Transversal motor, PWM pin
33	DOUT3	Transversal motor, DIR pin
34	DOUT4	TEC control
44	GATE1	Digital $+5\,\mathrm{V}$
45	CLK1	Axial motor, encoder B channel
47	GATE2	Digital $+5\,\mathrm{V}$
48	CLK2	Transversal motor, encoder B channel
49	$+5\,\mathrm{V}$	Power supply for the digital circuits
50	DIGGND	Digital ground

Table E.1. Pin assignment of the DAQCard-700

Appendix F.

Schematic

The schematic is divided into five sub-parts to fit onto the pages. These parts are namely

- the analogue part with the photo detector, the transimpedance amplifier, the band-pass filter and the variable non-inverting amplifier,

- the H-bridge that controls the axial motor,

- the H-bridge that controls the transversal motor,

- the 50 pin DAQCard-700 connector together with the control circuit for the TEC element and

- the power supplies of the integrated circuits and the power supply connectors.
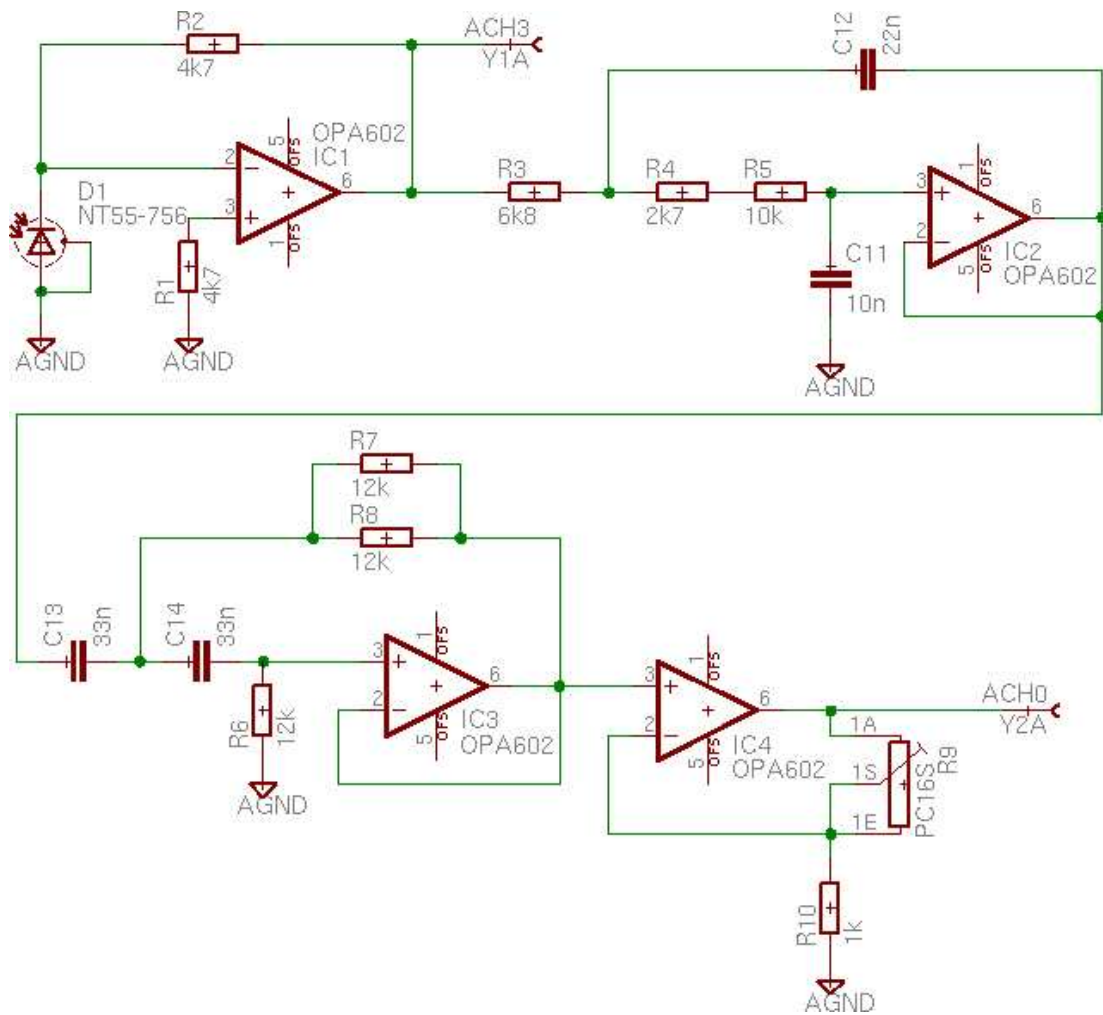
Figure F.1. Schematic: Analogue part
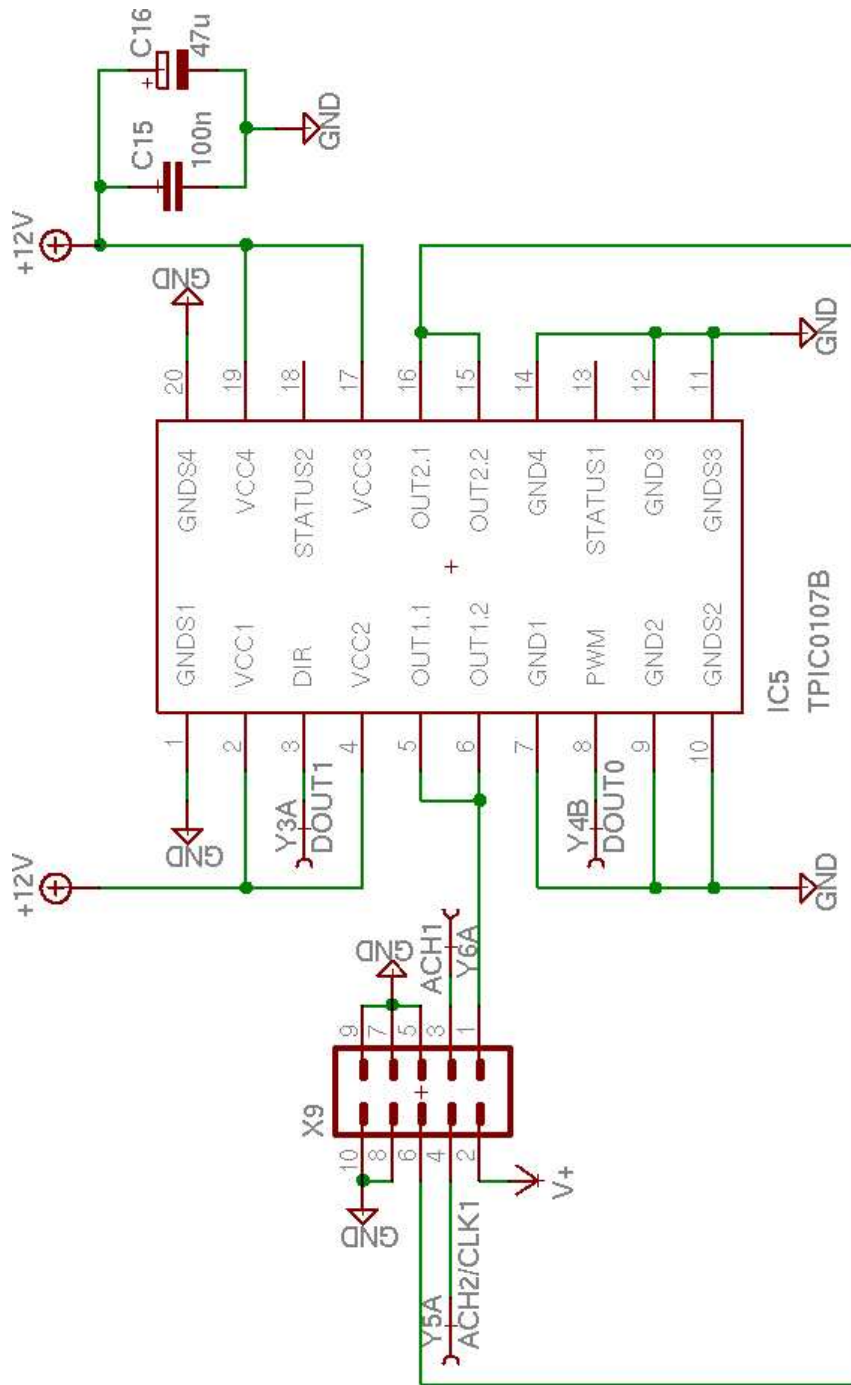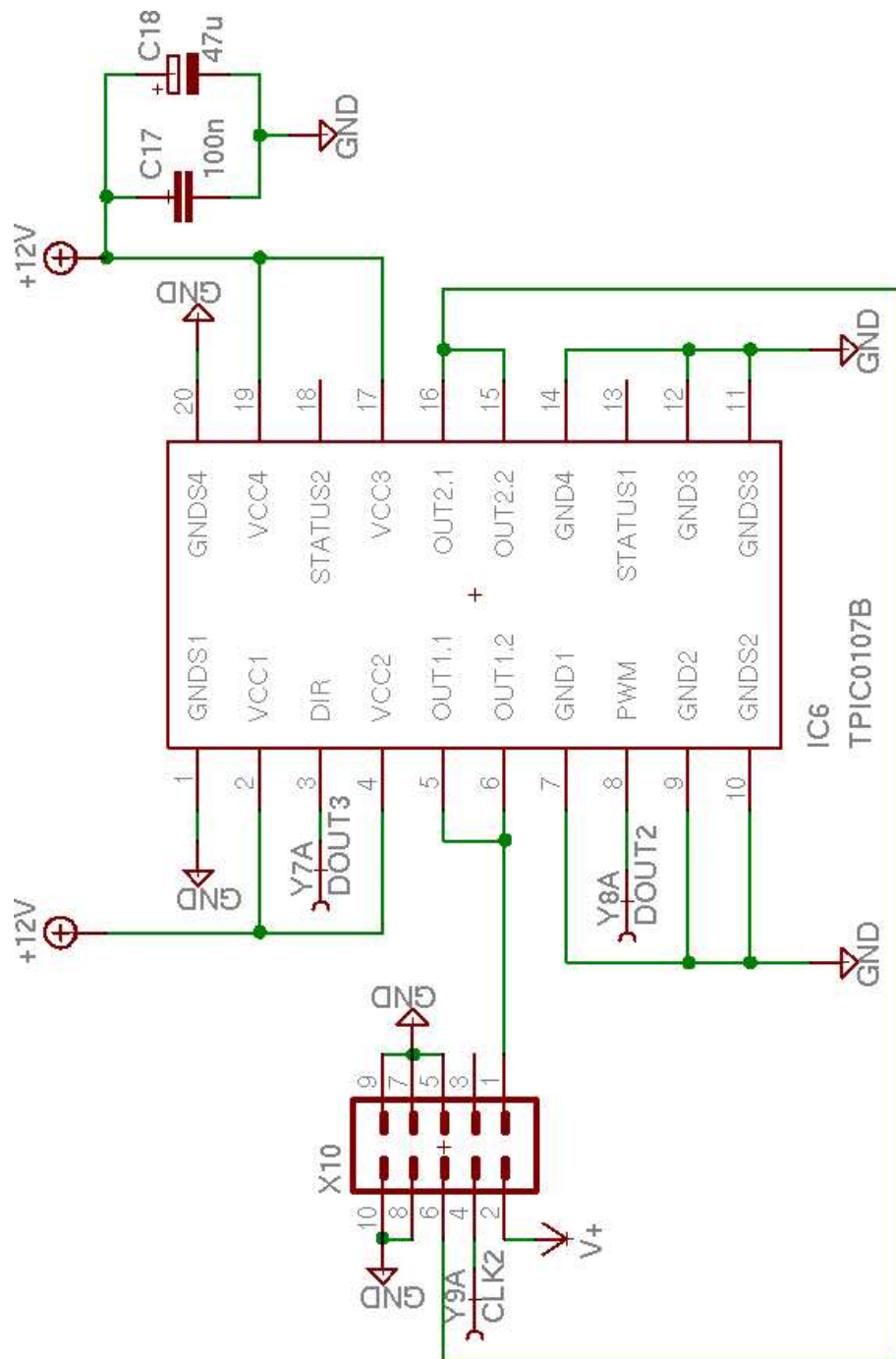
Figure F.2. Schematic: Axial motor control

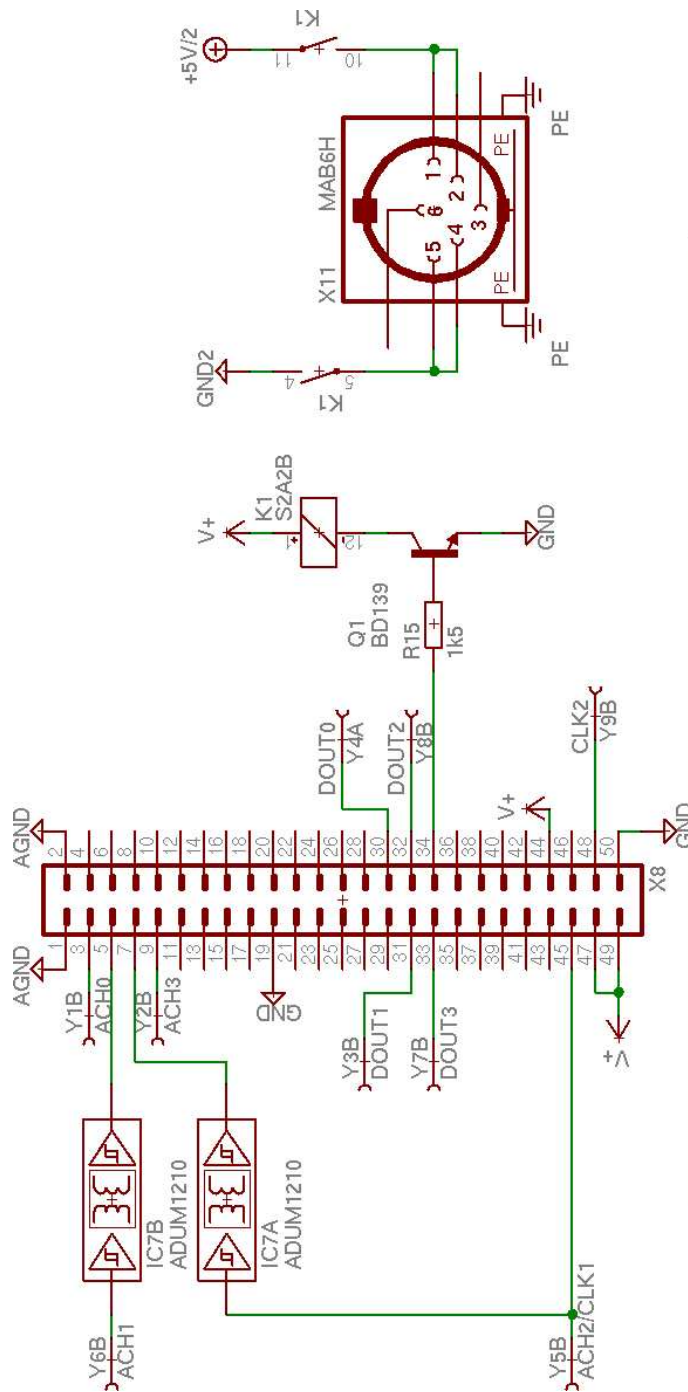Figure F.3. Schematic: Transversal motor control
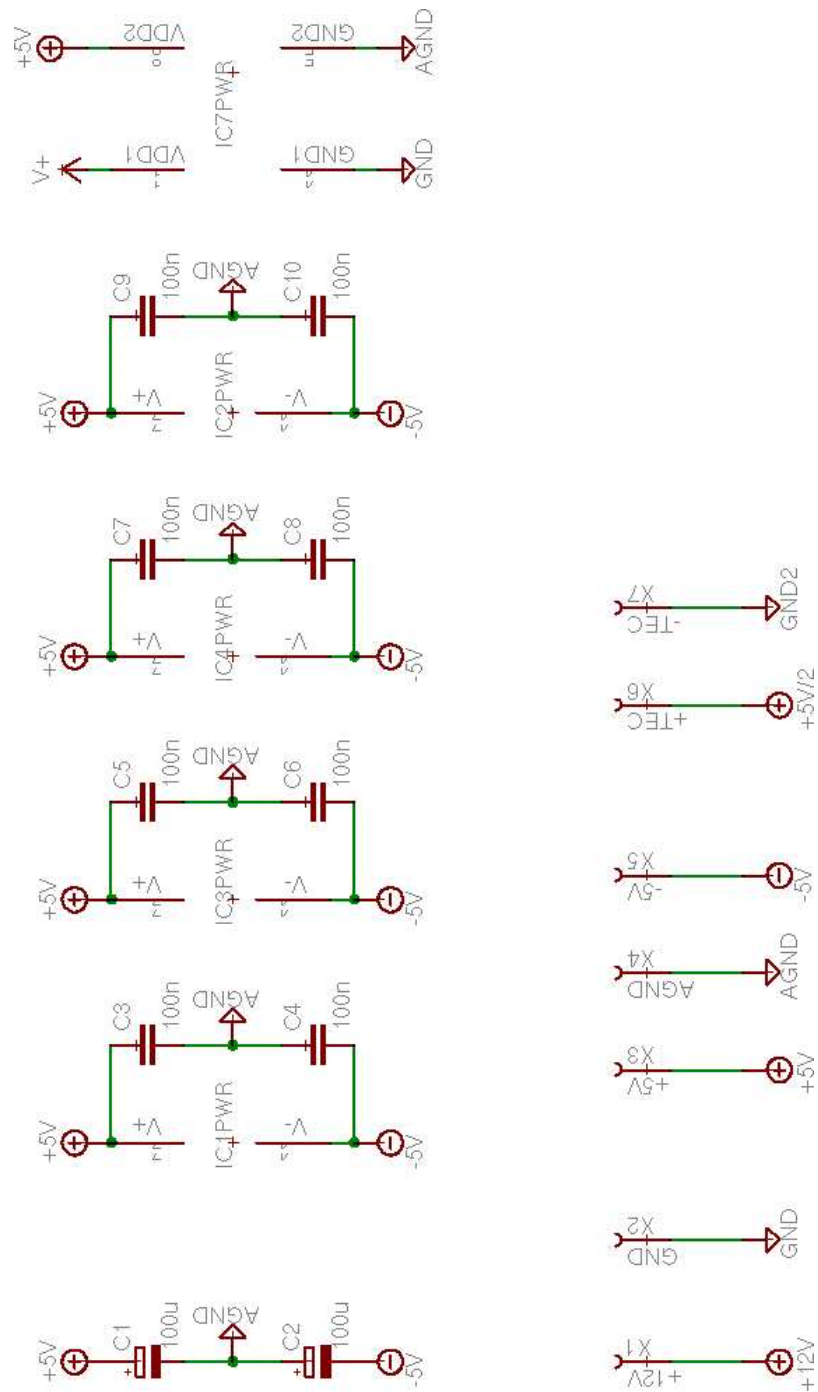
Figure F.4. Schematic: DAQCard-700 and TEC connector

Figure F.5. Schematic: Power supplies and connectors

Appendix G.

Adapter for a logarithmic amplifier

An adapter for the logarithmic amplifier AD8304 (Analog Devices, Inc., Norwood, USA) is proposed in this section.

To use this amplifier, IC_1 and R_2 (fig. F.1) have to be removed. Furthermore, pin 8 of IC_1 has to connected to digital ground. Then the adapter can be inserted into the socket of IC_1.
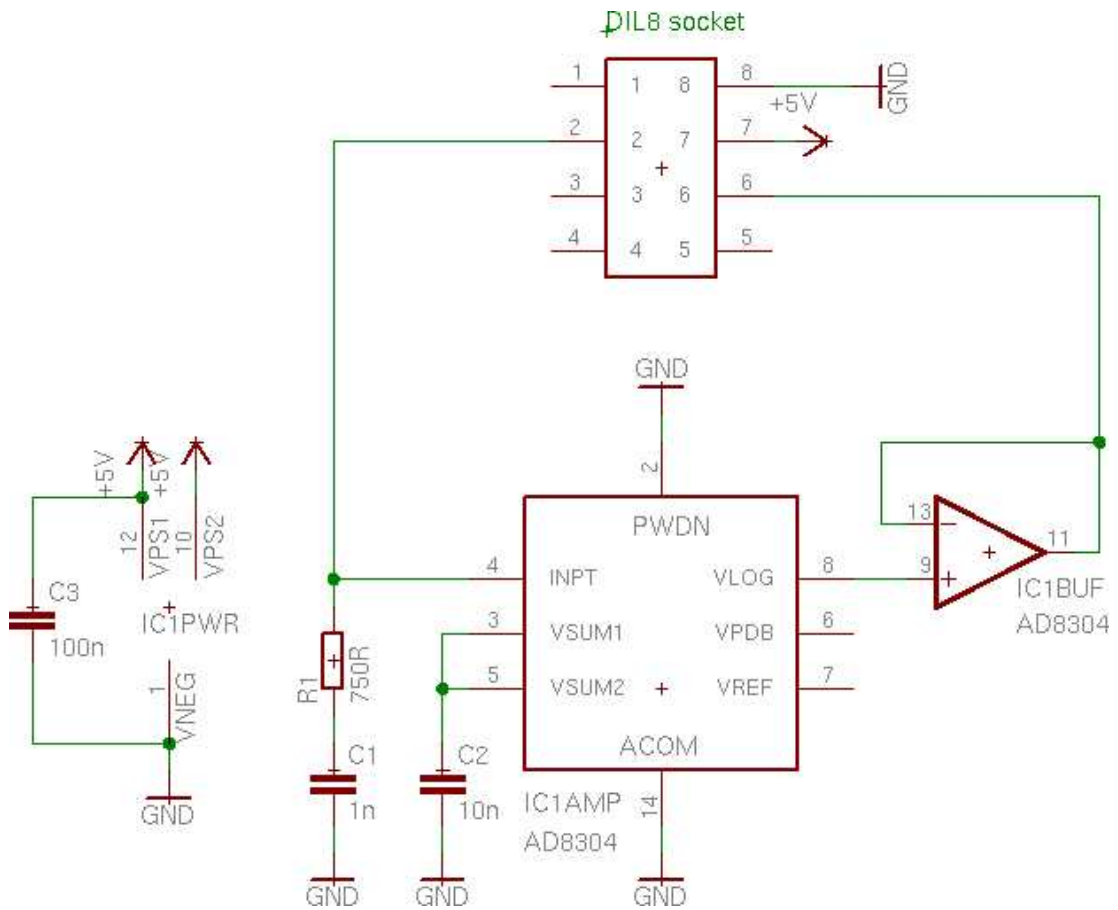

Figure G.1. PCB of an adapter for a logarithmic amplifier

Figure G.2. Schematic of an adapter for a logarithmic amplifier